



Evaluation of $\text{Pr}_2\text{Zr}_{2-x}\text{Ce}_x\text{O}_{7\pm\delta}$ pyrochlores as a potential Cu support catalysts for CO oxidation in simulated GDI conditions

Emerson Luiz dos Santos Veiga^{a,*}, Álvaro Díaz-Verde^b, Maria José Illán-Gómez^b, Héctor Beltrán-Mir^{a,*}, Eloísa Cordoncillo^{a,*}

^a Department of Inorganic and Organic Chemistry, University Jaume I, Av. Vicent Sos Baynat s/n 12071, Castellón de la Plana, Spain

^b MCMA Group, Department of Inorganic Chemistry and Materials Institute (IUMA), Faculty of Sciences, University of Alicante, Ap. 99, E-03080 Alicante, Spain

ARTICLE INFO

Keywords:

Pyrochlores
Copper
CO oxidation
Gasoline Direct Injection (GDI) engines

ABSTRACT

This study evaluates the catalytic activity, both as bulk catalysts and as supports for copper catalysts for CO oxidation in a simulated Gasoline Direct Injection Engine (GDI) of two pyrochlores: $\text{Pr}_2\text{Zr}_2\text{O}_7$ (PZ) and $\text{Pr}_2\text{Zr}_{1.9}\text{Ce}_{0.1}\text{O}_{7\pm\delta}$ (PZC). These pyrochlores were synthesized by the solvothermal method. XRD, FE-SEM, HR-TEM, XPS, H_2 -TPR, and O_2 -TPD characterization techniques were employed to determine the structural, microstructural, and redox properties of the samples. All materials exhibited high catalytic activity for CO oxidation, with Cu-PZC showing the best performance, which is comparable to that of a 1% Pt/ Al_2O_3 commercial catalyst used as a reference. Thus, the synthesized solids could be a promising and cost-effective alternative to noble metal-based catalysts used to control GDI exhaust gas composition.

1. Introduction

In the next few decades, the increasing energy demand will lead to a substantial growth in polluting gas emissions [1–5]. Consequently, the development of new technologies able to supply the energy demand, as well as to control polluting gas emissions, will be crucial. In fact, efficient and low-cost electrochemical energy storage and conversion technologies, such as electrolytic cells [6–8], regenerative fuel cells [9–11], and chemical looping technology [12–15], show potential as future energy sources. However, the slow kinetics of the essential electrochemical reactions restricts the widespread use of some of these technologies. Therefore, exploring highly active, stable, and economical catalysts and electrocatalysts at low and intermediate temperature conditions is essential to increase energy efficiency, reduce costs, and operation temperature [16–18].

Despite the advances in engine technology in recent decades, the combustion of gasoline is still not efficient enough, leading to exhaust gases containing significant amounts of unburned and partially burned hydrocarbons, and excessive amounts of CO [19–21]. The exhaust environment of an internal combustion engine is highly severe and differs significantly from the steady-state operation of most chemical plant catalytic processes. Therefore, the catalysts used in these engines must be able to operate at low temperatures to withstand thermal

excursions of up to 1000 °C, resist the presence of poisons, and remain unaffected by gas flow fluctuations and severe mechanical vibrations [22,23]. Moreover, one of the most significant issues consists in accomplishing the called "Target 150", which implies finding a catalyst able to achieve a 90% reduction in the emissions of gaseous pollutants, being CO among them, at a temperature of 150 °C [24].

Platinum-containing compounds are among the most extensively researched and effective catalysts [25–28]. The high number of studies dedicated to noble metal catalysts is due to their outstanding thermal stability, their lower propensity to react with support materials compared to base metals, and their capacity to handle high gas flows without poisoning. Nevertheless, the limited availability of noble metals (i.e., their high cost) and their insufficient durability hinder their use as catalysts in internal combustion engines [29–31].

To minimize the use of noble metals, transition metals, such as copper, could be an interesting alternative [32–34]. Copper-based catalysts are commonly employed in several reactions, including methanol reforming [35,36] and CO oxidation reaction [37–39], due to their excellent catalytic activity and cost-effective synthesis methods.

Thus, different copper catalysts have been proposed for CO oxidation, such as CuO powders [40–42], copper and manganese mixed oxides [43–46], or copper chromites [47]. This is because copper is able to activate CO by chemisorption, being metallic copper the most active

* Corresponding authors.

E-mail addresses: edossant@uji.es (E.L. dos Santos Veiga), mir@uji.es (H. Beltrán-Mir), cordonci@uji.es (E. Cordoncillo).

<https://doi.org/10.1016/j.apcatb.2023.123371>

Received 28 July 2023; Received in revised form 4 October 2023; Accepted 6 October 2023

Available online 7 October 2023

0926-3373/© 2023 Elsevier B.V. All rights reserved.

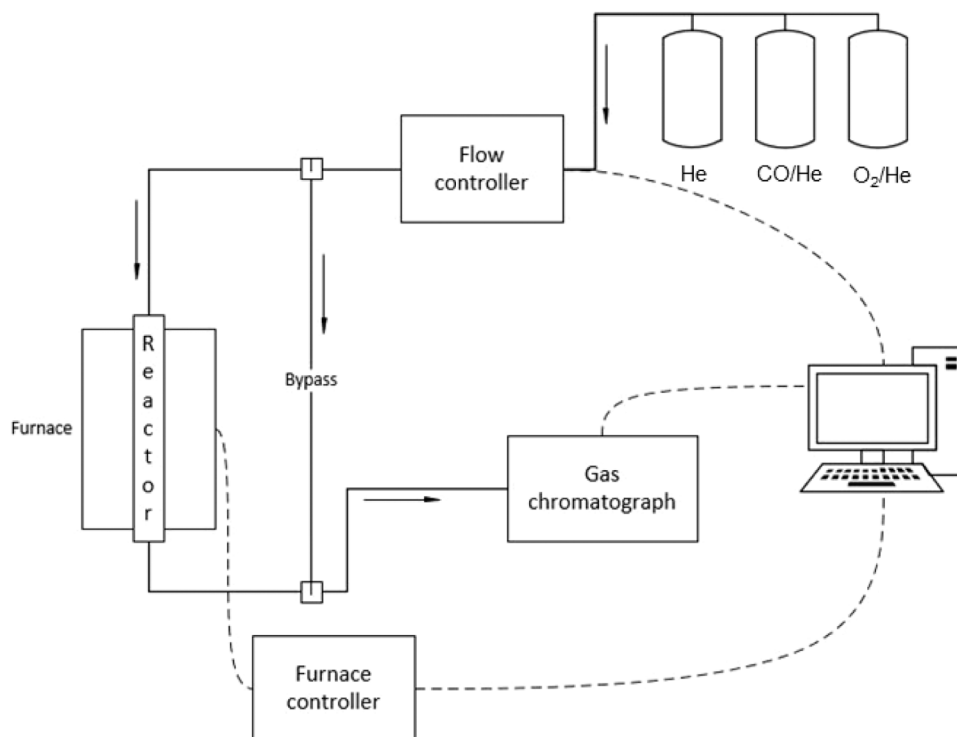


Fig. 1. Experimental setup for testing the CO oxidation reaction.

oxidation state followed by Cu(I) and Cu(II) [40]. However, these copper-based catalysts could present some drawbacks, such as poor stability, sintering and poisoning, which could cause the deactivation of the catalyst [36]. Consequently, one option to overcome these concerns is using active supports which can enhance not only the stability of the catalyst but also the dispersion of the active metals, thus increasing the catalyst performance. In this sense, among other options, the catalytic activity of Cu-based catalysts can be significantly enhanced by using copper-incorporated [48–52] and/or by supporting copper on perovskite [53], rare-earth metal oxides (REMOs) [54–58], and CeO₂ as active supports [47,59,60]. In this case, the promoting effects are attributed to the decrease in the bond energy between copper and oxygen and the increase in the mobility of oxygen. Moreover, REMOs used as additives can improve the thermal stability of catalysts based on transition metal oxides such as copper [61–65].

In this context, rare-earth pyrochlore-type structures (A₂B₂O₇) have been shown to be promising active supports [66–69]. The stable crystalline phase of this structure depends on the ratio between the ionic radius of the atoms located at A and B (r_A and r_B) sites. When the r_A/r_B ratio is in the range of 1.46–1.78, an ordered pyrochlore phase with a *Fd-3 m* space group is formed. In this structure, the A-site is typically occupied by ions with oxidation states + 2 or + 3, such as La, Pr, Sm, Ca, or Sr, among others, and they are surrounded by eight oxygen ions. On the other hand, the B-site is usually occupied by transition metals, such as Zr, Ti, or Nb, with oxidation states + 4 or + 5, and they are six-fold coordinated with oxygen [70–72].

Rare-earth pyrochlore solids offer numerous advantages, such as high thermal and chemical stability, high oxygen mobility, inherent oxygen vacancies, and high ionic mobility. Based on these properties, they have been used for different applications [70–77], including the purification of exhaust gases generated by automotive vehicles and industrial engines. In a previous study [77], Fe-doped Pr₂Zr₂O₇ pyrochlore showed interesting catalytic properties for the CO oxidation reaction, and its performance was improved by increasing the dopant amount in the structure, since more defects and oxygen vacancies were created allowing a higher redox activity.

Therefore, the objective of this work is to evaluate the activity of pyrochlores with Pr₂Zr_{2-x}Ce_xO_{7±δ} ($x = 0$ and 0.1) composition as catalysts or supports for copper-based catalysts for the CO oxidation in simulated Gasoline Direct Injection (GDI) engines, in order to determine the use of these solids as potential catalysts for the control of CO emissions.

2. Experimental

2.1. Synthesis and characterization of catalysts

Two nominal compositions (Pr₂Zr₂O₇ and Pr₂Zr_{1.9}Ce_{0.1}O_{7±δ}, referred as PZ and PZC, respectively) were prepared by the solvothermal method [77]. Pr(CH₃COO)₃·X H₂O (Sigma-Aldrich, 99.9%), ZrOCl₂·8 H₂O (Sigma-Aldrich, 98%), and Ce(NO₃)₃·6 H₂O (Sigma-Aldrich, 99%) were used as precursors. These precursors were first dissolved in 50 mL of distilled water, and the pH of the solution was adjusted to 10 using ammonia solution (Scharlab, 32% w/w). The resulting suspension was vigorously stirred for 10 min and transferred to a Teflon-lined vessel with a volume of 125 mL. The total volume of the solution was approximately 80 mL. The Teflon vessel was then placed in a digestion bomb and heated in an oven at 180 °C for 24 h. After cooling, the suspensions were dried at 100 °C for 24 h. Finally, the resulting powders were calcined in air at 1200 °C for 2 h with a heating rate of 5 °C min⁻¹.

For copper addition, the incipient wetness impregnation method was employed, which consists in saturating the support with a solution of Cu(NO₃)₂·3 H₂O, with a concentration adjusted according to the required amount of copper (4% wt) [53]. The wet catalyst was then stirred at room temperature for 24 h, followed by drying at 80 °C for 24 h. Finally, the catalyst was calcined at 800 °C for 4 h. The impregnated samples were referred as Cu-PZ and Cu-PZC.

The raw (PZ and PZC) and impregnated samples (Cu-PZ and Cu-PZC) were deeply analyzed using the following characterization techniques.

For X-Ray Diffraction (XRD) analysis, a Bruker-AX D8-Advance X-ray diffractometer with Cu-K_α radiation was used. The data were collected at room temperature within the range of 10° ≤ 2θ ≤ 70° with a step size of

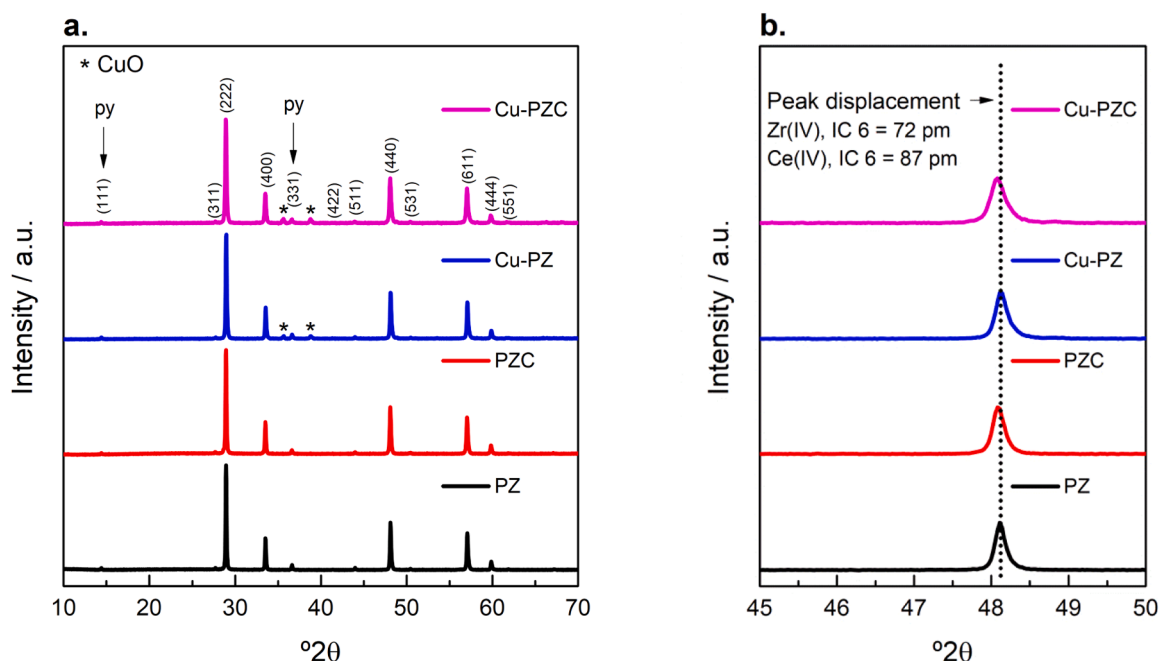


Fig. 2. (a) X-ray diffraction (XRD) patterns for $\text{Pr}_2\text{Zr}_{2-x}\text{Ce}_x\text{O}_{7\pm\delta}$ samples ($x = 0$ and 0.10) of the raw samples (PZ and PZC) and Cu-impregnated samples (Cu-PZ and Cu-PZC). (b) The (440) diffraction peak of the pyrochlore phase for all compositions.

0.03° and a counting time of 1 s for each step. The crystallite size was obtained using Scherrer equation, according to the literature [78].

The N_2 adsorption isotherms were carried out on a Micromeritics Gemini V equipment, being the specific surface area and the pore size calculated using the multipoint Brunauer-Emmett-Teller (BET) and the Barrett-Joyner-Halenda (BJH) methods, respectively. Prior to the adsorption analysis, each sample was degassed for three hours at 150°C .

The microstructure and morphology of samples were analyzed employing a JEOL 7001 F Field-Emission Scanning Electron Microscope (FE-SEM) with an acceleration voltage of 15 kV. The samples were coated with platinum and deposited on an aluminum holder. For High-Resolution Transmission Electronic Microscopy (HR-TEM), a JEOL 2100 equipment was used, which is equipped with a JEOL EM-24830FLASH digital camera with a CMOS sensor, offering a resolution of $2\text{ k} \times 2\text{ k}$. The microscope was also equipped with a STEM DF/BF image acquisition system with a resolution of 1 nm.

To carry out the X-ray Photoelectron Spectroscopy (XPS) measurements, a Thermo-Scientific K-Alpha Photoelectron Spectrometer with an Al K_α (1486.7 eV) radiation source was used. XPS spectra were obtained by maintaining the pressure of the analysis chamber at 5×10^{-10} mbar. To correct the binding energy shifts, caused by surface charging, the adventitious carbon component in the C 1 s region at 284.8 eV was aligned (see Fig. 1Sa in Supplementary Information). The XPS data were analyzed using CasaXPS software. All curves were deconvoluted using a 50% Gaussian/50% Lorentzian function with the ratio between the peaks fixed according to the degeneracy of each spin state. To obtain proper fitting of the curves, area and FWHM constraints were applied.

The reducibility of the catalysts was evaluated through Temperature Programmed Reduction with H_2 (H_2 -TPR) experiments, using a Pulse Chemisorb 2705 instrument (from Micromeritics) equipped with a Thermal Conductivity Detector (TCD). About 30 mg of the sample were subjected to a heating rate of $10^\circ\text{C min}^{-1}$ from 25°C to 950°C (being the corresponding H_2 -TPR profiles presented till 500°C , since there are no relevant signals detected at higher temperatures than 500°C) in a 5% H_2/Ar atmosphere (40 mL min^{-1}). The quantification of the amount of H_2 consumed during the experiments was obtained using a CuO reference sample.

For Temperature Programmed Desorption of O_2 (O_2 -TPD)

experiments, 16 mg of sample was heated using a heating rate of $10^\circ\text{C min}^{-1}$ from room temperature to 950°C under a helium flow of 100 mL min^{-1} . The evolved gases were monitored by a TG-MS system (Q-600-TA and Thermostar from Balzers Instruments, Pfeiffer Vacuum GmbH, Germany), detecting 18, 28, 32, and 44 m/z signals (for H_2O , CO, O_2 , and CO_2 , respectively). The amount of evolved oxygen was estimated using CuO as a reference sample.

2.2. Catalytic activity

Temperature Programmed Reaction (CO-TPR) experiments have been developed to determine the catalytic activity for CO oxidation. In order to simulate the composition of GDI engine exhaust, two reactant mixture have been used (100 mL min^{-1}): i) a low CO concentration reactant mixture, with 0.1% CO and 1% O_2 in He, selected to avoid any potential competition of the reactants for the active sites of the catalysts due to their low concentration, and ii) a near stoichiometric reactant mixture, consisting of 1% CO and 1% O_2 in He, which simulates the CO concentration in the actual Three-Way Catalyst (TWC) working conditions. For the experiments, 50 mg of catalyst and 100 mg of SiC were loaded into a U-shaped quartz reactor and a heating rate of $10^\circ\text{C min}^{-1}$ from room temperature to 500°C was applied. The most active catalysts were also tested in the near stoichiometric reactant mixture at 300°C for 3 h, and the recyclability of the catalysts was determined by conducting two consecutive reaction cycles at this temperature. For the detection and quantification of the reaction products, an Agilent 8860 Gas Chromatograph, equipped with a Thermal Conductivity Detector and two packed columns (Porapak-Q and MolSieve-13X), was used. Figure 1 shows a scheme of the experimental setup.

The CO conversion was determined using the following equation:

$$\chi_{\text{CO}}(\%) = \frac{n_{\text{CO},\text{in}} - n_{\text{CO},\text{out}}}{n_{\text{CO},\text{in}}} \cdot 100 \quad (1)$$

where $n_{\text{CO},\text{in}}$ is the inlet molar flow rate of CO, and $n_{\text{CO},\text{out}}$ is the outlet molar flow rate of CO which has not been oxidized to CO_2 .

Table 1

Specific surface area and pore diameter values determined by the BET and BJH methods, respectively. Average particle size estimated using SEM micrographs. Crystallite size obtained from XRD data using Scherrer's equation at peak (440).

Sample	Specific Surface Area (m ² /g)	Pore Diameter (Å)	Average particle size (nm)	Crystallite size (nm)
PZ	8	20	144	59
PZC	6	21	153	52
Cu-PZ	1	20	168	54
Cu-PZC	1	21	185	48

3. Results and discussion

3.1. Composition, textural and structural properties

Fig. 2 shows the diffractograms of the four synthesized samples. The

results revealed that both copper-free samples (PZ and PZC) exhibited a single-phase $\text{Pr}_2\text{Zr}_{2-x}\text{Ce}_x\text{O}_{7\pm\delta}$ pyrochlore structure with $Fd-3m$ space group (JCPDS-ICDD 19-1021), as evident from the pyrochlore characteristic peaks at approximately 14° (111) and 37° (331). The superstructure reflections in the XRD patterns are consequence of the necessary perturbations to form the pyrochlore structure from a fluorite arrangement, arising from factors such as the radiation scattering difference of species occupying the *A* and *B* cation sites, oxygen displacement from the ideal position, and the distribution of oxygen vacancies [79].

As seen in Fig. 2b, in the Ce-doped sample (PZC), the (400) peak of pyrochlore shifts toward lower 2θ angles compared to PZ. This fact is due to the unit cell expansion caused by the incorporation of Ce, which is related to the difference between the ionic radii of Zr(IV) ($r = 72$ pm, for 6 coordination number (CN)) and of Ce(IV) ($r = 87$ pm, CN = 6) [80]. The peak displacement is in agreement with the Bragg's Law ($n\lambda = 2d \cos\theta$, where d is the interplanar distance, θ is the diffraction angle, and λ is the wavelength of the incident radiation). Furthermore, the

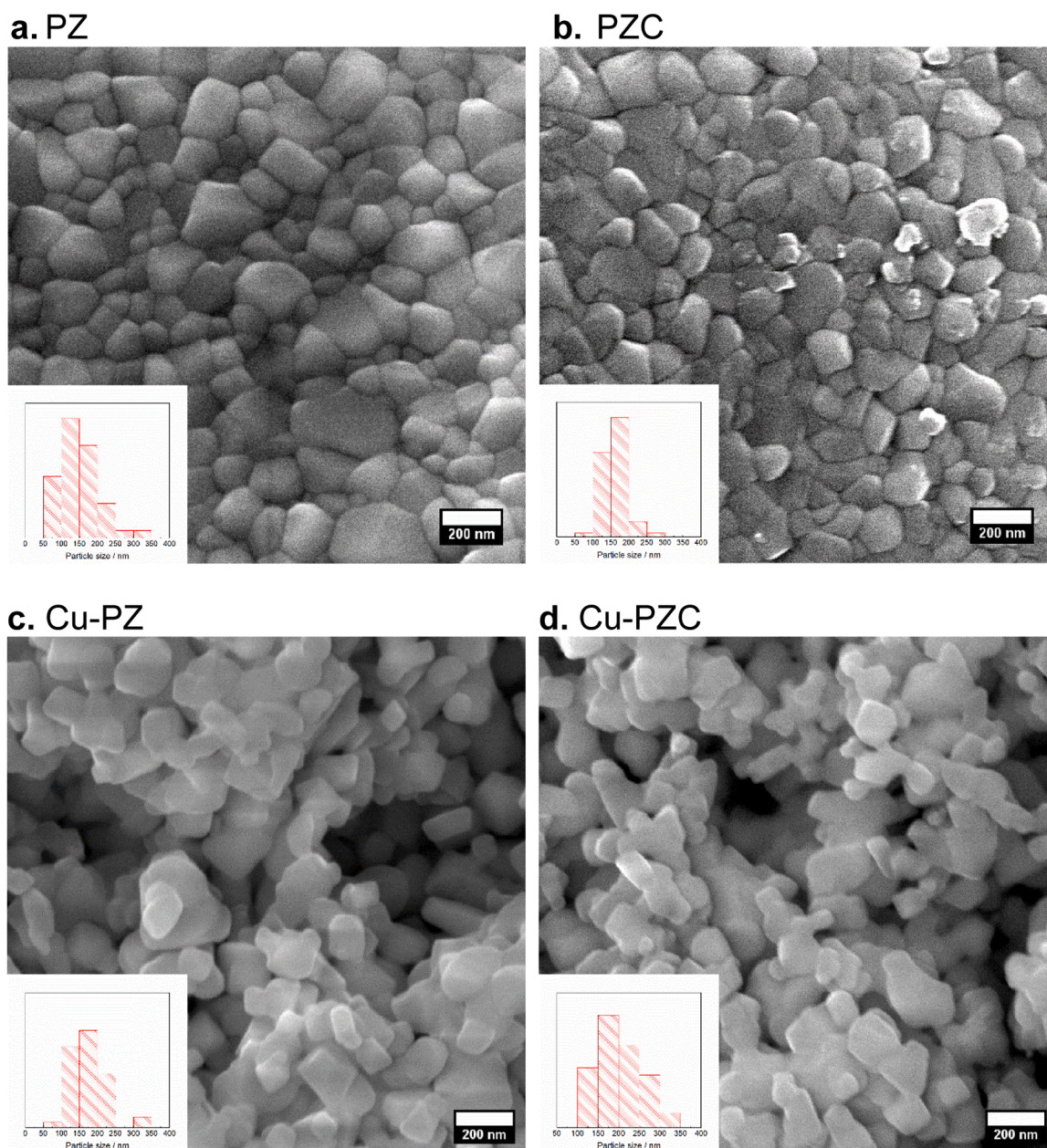


Fig. 3. FE-SEM micrographs of the (a) PZ, (b) PZC, (c) Cu-PZ, and (d) Cu-PZC samples. Particle size distribution is inserted in each image.

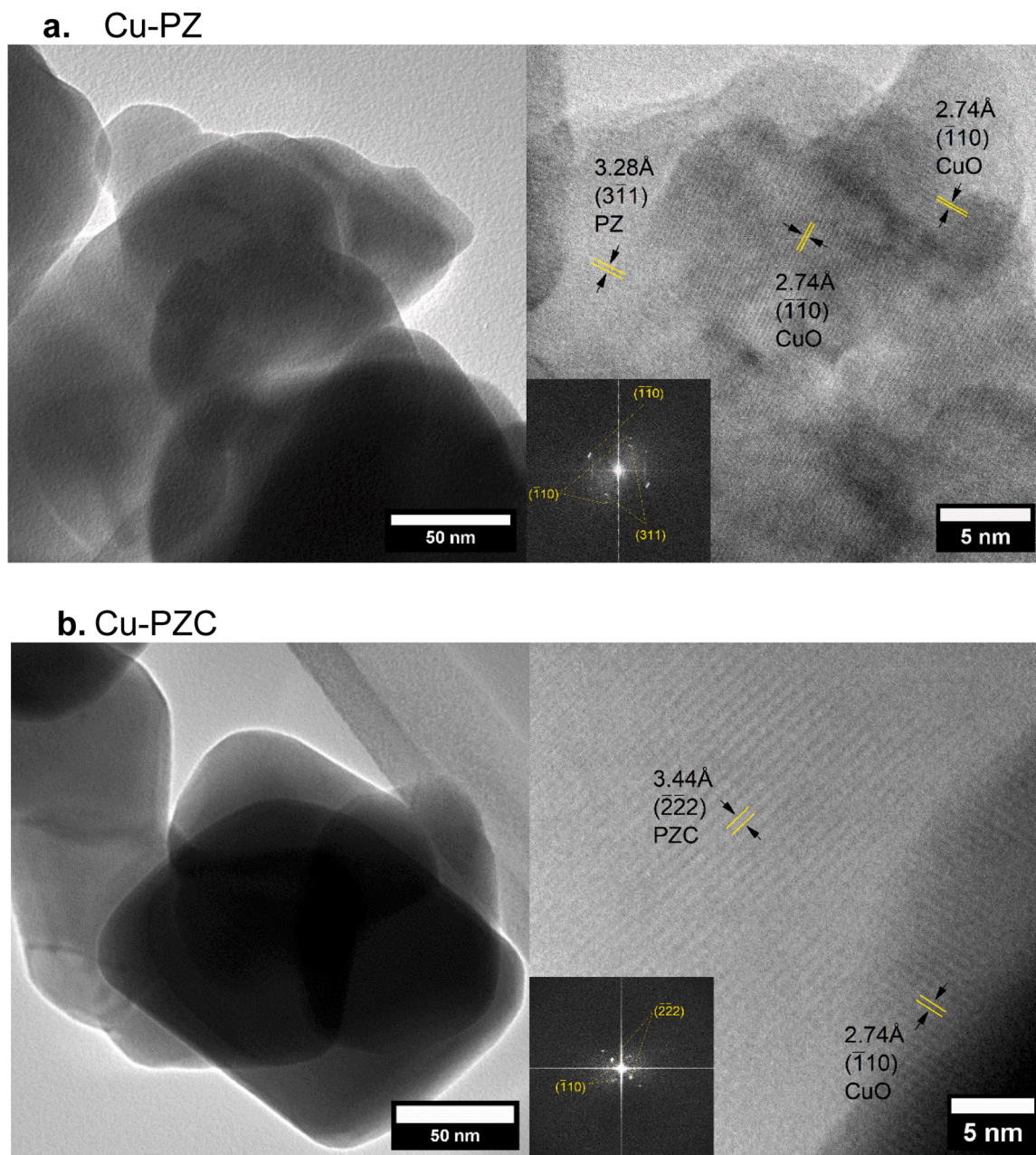


Fig. 4. High-resolution TEM images of (a) Cu-PZ and (b) Cu-PZC. The planes seen in the figures are labelled. The inset shows the FFT diffraction patterns of the surfaces.

diffractograms of the Cu-impregnated samples revealed the presence of CuO (JCPDS-ICDD 74–1021), as the corresponding 2θ peaks at 35.7° and 38.9° were detected. As shown in Table 1, the crystallite size was similar for all samples, with a slight decrease observed in the Cu-impregnated samples.

FE-SEM micrographs, shown in Fig. 3 for PZ and PZC samples, exhibit particles sizes averaging about 200 nm (see the inserted graphs of particle size distribution in each figure). Note that there is no significant difference between PZ and PZC in terms of particle size and morphology. The copper-impregnated samples, Cu-PZ and Cu-PZC (Figs. 3c and 3d respectively), exhibit some particle sintering, likely due to the thermal treatment carried out after the impregnation step, resulting in a slight increase in the average particle size (see Table 1). As no significant differences between FE-SEM images for PZ/PZC and Cu-PZ/Cu-PZC are observed, the CuO species should be well dispersed on the supports.

The copper-impregnated samples were additionally analyzed by HR-TEM, being the results shown in Fig. 4. The HR-TEM analysis revealed the presence of isolated copper oxide nanoparticles on PZ and PZC supports, as can be observed in the inserted FFT treatment included in the figures.

Figs. 4a and 4b reveal the presence of different particles with approximate sizes ranging between 50 and 150 nm for PZ and PZC, respectively. Even though an accurate EDX study was not possible because of the overlapping of the PZ/PZC and CuO phases, which made it difficult to obtain high-quality signals, the crystal planes referred to the support material and CuO were identifiable (see enlarged images on the right). In Fig. 4a, corresponding to the Cu-PZ (311) planes, an interplanar distance of 3.28 Å is observed, which is similar to the expected theoretical distance of 3.22 Å (JCPDS-ICDD 19–1021). Additionally, the (110) CuO crystal plane was observed, with a distance of 2.74 Å, which is almost identical to the theoretical value of 2.737 Å

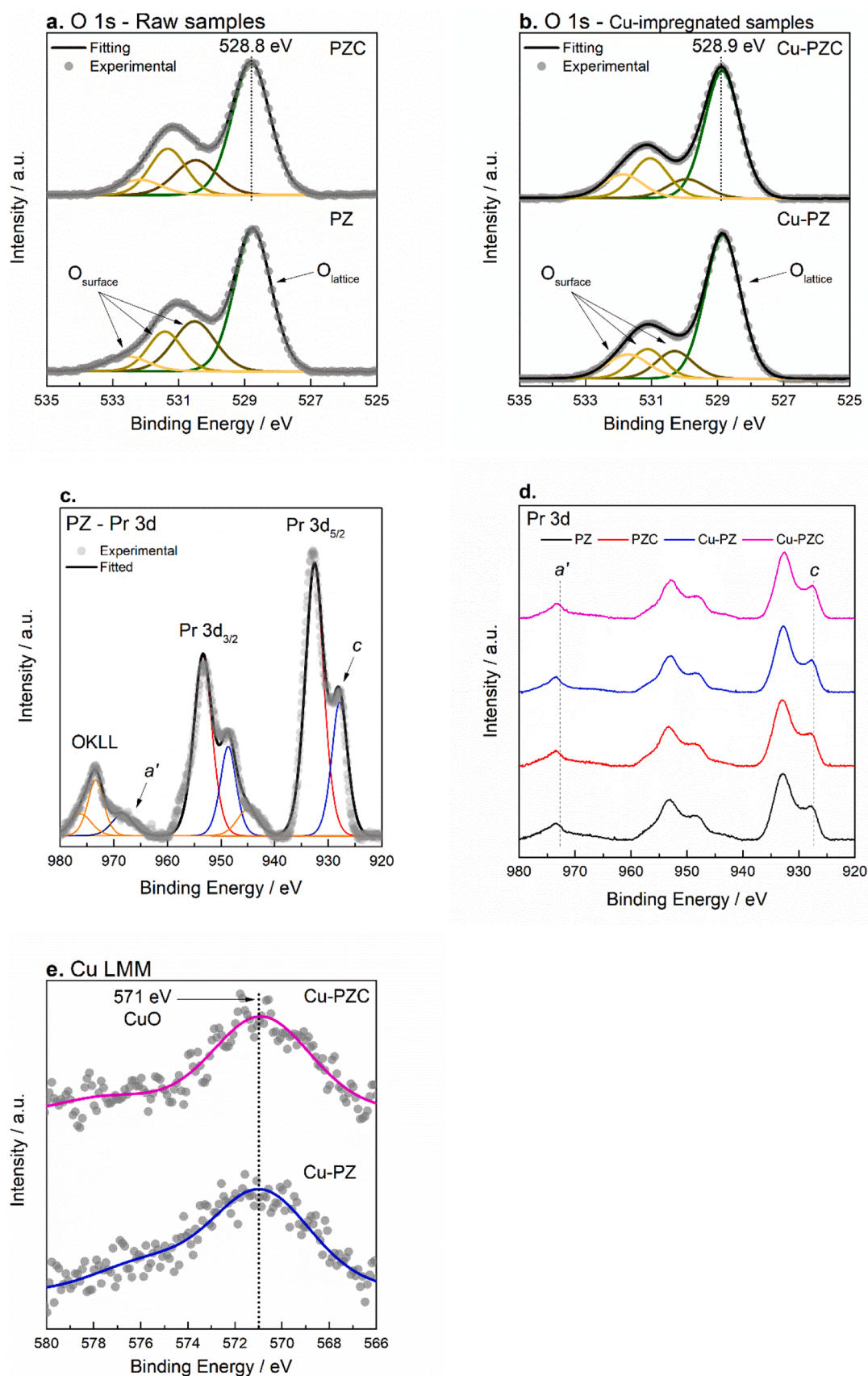


Fig. 5. XPS spectra of the (a and b) O 1s, (c and d) Pr 3d, and (e) Cu LMM regions for the raw and Cu-impregnated samples.

Table 2

Peaks contribution (%) in the O 1 s region.

Sample	O _{surface}	O _{lattice}	O _{surface} / O _{lattice}
PZ	43.75	56.25	0.78
PZC	42.93	57.07	0.75
Cu-PZ	37.00	63.00	0.59
Cu-PZC	38.27	61.73	0.62

(JCPDS-ICDD 74-1021). In Fig. 4b, the corresponding Cu-PZC (110) CuO crystal plane was also detected, being the interplanar distance identical than the corresponding to Cu-PZ. Moreover, the (222) plane of the PZC structure with an interplanar distance of 3.44 Å was found. This value is greater than the theoretical value of 3.09 Å, confirming the insertion of Ce in the pyrochlore structure, as it was previously observed by XRD.

Table 1 also includes the specific surface area (S_{BET}) and mean pore diameter for both the raw and impregnated samples. As expected, all samples exhibit low S_{BET} values [77]. Furthermore, following the incorporation of Ce, a decrease in S_{BET} values is observed. The average pore diameter of the two supports corresponds to nanopores, and no significant effect of Ce incorporation was detected. After impregnation with copper, the samples exhibited very low specific surface areas. This can be attributed to sintering during the heat treatment following the impregnation step, a phenomenon also observed through FE-SEM analysis (Figs. 3c and 3d). Similar pore diameters were also obtained.

3.2. Surface composition: XPS

To identify the different chemical species present on the surface of the samples, X-Ray Photoelectron Spectroscopy (XPS) technique was employed. Fig. 1 S in Supplementary Information shows the XPS survey spectra for the raw and impregnated samples, where the main core-level peaks corresponding to the elements present on the surface of the material are labeled.

In the XPS spectra of the O 1 s region of raw samples (Fig. 5a), two peaks are detected: i) the main peak appearing at 528.8 eV corresponds to the oxygen atoms present on the surface lattice (O_{lattice}) and ii) the second broad peak located at 531 eV corresponds to surface oxygen (O_{surface}), which can be deconvoluted into three peaks centered at, approximately, 530.7 eV, 531.5 eV, and 532.5 eV, that correspond to oxygen surface adsorbed species [53,81–83], such as metal carbonates, carbonyl and hydroxyl species.

The data in Table 2 reveal that, for the two raw samples (PZ and PZC), the area of the O_{lattice} peak is higher than the area of O_{surface} peak, indicating a predominance of lattice oxygen on the surface. By comparing the area of the two peaks, a significant difference in the amount of oxygen adsorbed species for the two compositions is not observed, as the ratios between the O_{lattice} and O_{surface} peaks are similar. So, assuming that the adsorption of oxygen species occurs preferentially in oxygen vacancies, it seems that the amount of oxygen vacancies in both samples is similar [84,85].

For copper-impregnated samples, Cu-PZ and Cu-PZC (Fig. 5b), the highest peak area also corresponds to O_{lattice}, and a similar O_{surface}/O_{lattice} ratio is found for the two compositions. Comparing with the raw samples (Fig. 5a), it is observed that the area of the peak corresponding to the adsorbed species (O_{surface}) is lower in the presence of copper (Table 2), so, it means that the surface of the support has been modified by the presence of CuO, thus affecting the availability and accessibility to oxygen adsorption sites. Note that the increase in the O_{lattice} peak area is an evidence of the existence of CuO deposited on the surface of supports.

Fig. 5c displays the XPS spectra in the Pr 3d region of PZ sample, where the oxygen Auger peak (OKLL) and the Pr 3d_{3/2} and Pr 3d_{5/2} core levels were detected [86], as has already been found in other studies [86–88]. Note that the peaks attributed to the Pr(III) (c) and Pr(IV) (a')

Table 3

Peaks contribution (%) in the Pr 3d region.

Sample	Pr 3d		
	Pr (IV)	Pr (III)	Pr (IV)/Pr (III)
PZ	3.18	14.95	0.21
PZC	3.10	15.61	0.20
Cu-PZ	2.82	16.07	0.17
Cu-PZC	2.49	16.57	0.15

species were identified (Fig. 5d) for all samples. As revealed by the data in Table 3, obtained by deconvoluting each spectrum and determining the area of each peak, Pr(III) is the predominant oxidation state for all samples, with a slightly higher relative contribution of the Pr(IV) peak in the raw samples. This conclusion agrees with the observed for the O 1 s XPS spectra, in which a lower amount of adsorbed oxygen is detected in the Cu-impregnated samples.

The Ce 3d region spectra for PZC and Cu-PZC samples (not shown) displayed noticeable dispersion, thereby increasing the complexity of the analysis, and making the identification of oxidation states and their contributions challenging. Additionally, it has to be taken into account that, in the presence of Pr, the reliable assignment of XPS peaks of Ce species cannot be done as the XPS peaks for Pr(III)/Pr(IV) also appear in the same 3d region [89]. Nevertheless, based on the literature, the coexistence of Ce(IV) and Ce(III) oxidation states on the surface of catalysts could be assumed [90–94].

Fig. 5e shows the Auger peak in the Cu L₃M_{4,5}M_{4,5} region for the two Cu-impregnated samples. This region of the XPS spectrum has been used to identify the copper species since, as it was previously indicated, the Cu 2p region also overlaps with the Pr 3d XPS signals, making difficult their visualization and interpretation, due to the higher amount of Pr with respect to Cu. According to literature, in the Cu L₃M_{4,5}M_{4,5} region, Cu⁰ exhibits a fine and well-resolved peak at approximately 568 eV, whereas copper oxides display broad and less resolved peaks at approximately 570 eV for Cu₂O and 569 eV for CuO [95]. In Fig. 6e, the XPS spectra for both samples present a broad peak with a maximum at 571 eV, which seems to correspond to copper oxides even though the position is slightly different from the expected [96,97]. This fact could be considered as evidence of the interaction between CuO and the pyrochlore support [98]. Thus, in agreement with the data obtained from the XRD and TEM analyses, it is suggested that the predominant oxidation state on surface is also Cu(II).

3.3. REDOX PROPERTIES: H₂-TPR AND O₂-TPD

To analyze the reducibility of samples, Temperature Programmed Reduction experiments using H₂ (H₂-TPR) were conducted. Fig. 6 shows the hydrogen consumption profiles for the four samples and for a CuO reference sample.

The reduction profile of the PZ sample shows two peaks corresponding to the reduction of Pr(IV) to Pr(III), appearing at slightly lower temperatures than those referenced in the literature (250–600 °C) [99, 100]. The first peak, at 268 °C, corresponds to the reduction of Pr(IV) to Pr(III) on the surface, and the second peak, at 394 °C, is assigned to the reduction of Pr(IV) species on the bulk. The PZC sample displays also two peaks at 312 °C and at 373 °C. Note that, as the first peak appears at higher temperatures than for PZ, it seems that, in the presence of Ce in the structure, the reduction of Pr(IV) on the surface is more difficult. The shift of the reduction peaks when Ce is present as a dopant, also reported for other structures [101–103], is usually associated with the interaction between the different chemical species. On the contrary, the second reduction peak appears at lower temperatures than for PZ, indicating an improvement in the reduction of bulk Pr(IV) as consequence of the weakening of the Pr-O or Zr-O bond [104–106]. Consequently, these peaks are closer in temperature than for PZ sample.

For PZC, according to literature [107–109], a contribution due to the

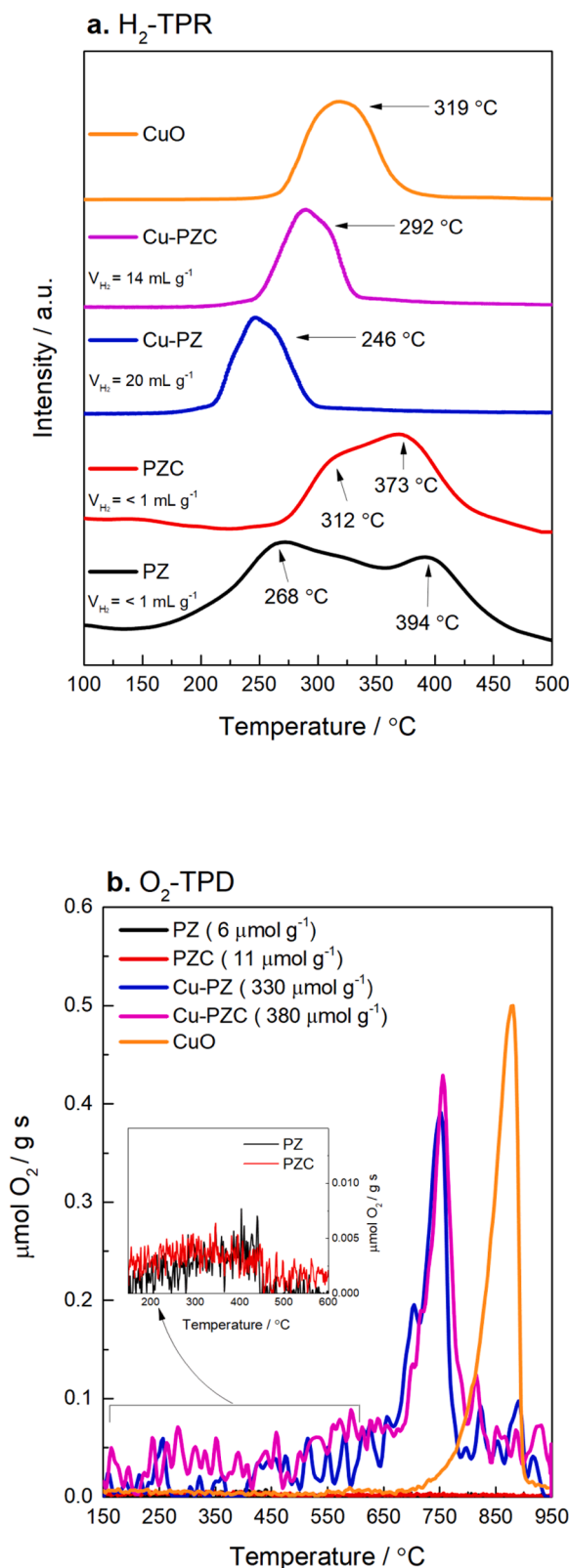


Fig. 6. (a) Normalized H₂-TPR consumption profiles for all samples. The H₂ consumption was calculated using a standard CuO sample and is expressed as mL of H₂ consumed per g of catalyst. (b) O₂-TPD profiles for all samples and for CuO used as reference.

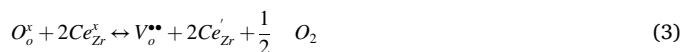
surface reduction of Ce(IV) to Ce(III) could be expected at around 200 °C. However, this peak is not observed in the PZC and Cu-PZC profiles. This is probably attributed not only to the very low amount of cerium on the samples, but also because of the higher redox potential of Pr(IV) to Pr(III), 2.7 V, compared to the one of Ce(IV) to Ce(III), 1.7 V, which could hinder the reduction of cerium [110]. Finally, the desorption/reduction of highly unstable surface oxygen species [100,111] could also take place during the H₂-TPR tests at low temperatures.

The calculated H₂ consumption, included in Fig. 6a, shows that the raw samples have a low degree of reducibility, which is expected since the pyrochlore structure contains Pr(III) as main oxidation state [86] and Ce(IV) is present in low concentration. The copper-impregnated samples display a higher H₂ consumption, showing more defined reduction peaks with maximums at around 246 °C for Cu-PZ and 292 °C for Cu-PZC, that correspond to the reduction of Cu(II) species [112,113], which takes place at lower temperatures in Cu-PZ sample than in Cu-PZC. Note that, as expected for Cu-supported samples, and because the dispersion of CuO on the supports facilitates the reduction process [53], these reduction peaks appear at lower temperatures than the observed for the reference CuO sample.

The O₂-TPD profiles displayed in Fig. 6b illustrate that Cu-PZ and Cu-PZC samples exhibit higher O₂ desorption than raw samples, PZ and PZC. For raw samples, the O₂ desorption is detected within the temperature range of 200–500 °C (shown in the enlarged zone in the figure). This desorption is likely associated with the release of oxygen coming from the chemically adsorbed on the surface (named α -O₂) [82,114] and on the surface lattice defects (designed as α' -O₂), being associated mainly with the reduction of surface Pr(IV), which also takes place in this temperature range [77,86,115].

For the copper-impregnated samples, the main O₂ desorption peak is observed at a temperature higher than 650 °C, corresponding to the release of lattice oxygen (designed as β -O₂), which seems to be mainly associated with the reduction of Cu(II) species to Cu(I) in the bulk of samples [53]. This finding agrees with the higher proportion of the O_{lattice} detected by XPS in the O 1 s region for these samples (Fig. 5b).

For the reduction of Pr(IV) and Ce(IV), as well as for the oxidation of oxide ions, the Kröger-Vink reactions have been proposed:



Where O_o^x is referred to oxygen atoms placed in the oxygen sites of the crystalline structure, Pr_{Pr}^x to Pr(IV) ions in Pr sites in the lattice, V_o^{••} to oxygen vacancies, Pr_{Pr}['] to Pr(III) ions placed in their sites [116], Ce_{Zr}^x and Ce_{Zr}['] to Ce(IV) and Ce(III) ions located in Zr sites, respectively, and e' to electrons.

Finally, to corroborate that oxygen desorption at higher temperatures is mainly due to the reduction of the CuO phase, the O₂-TPD profile of a CuO reference sample was included in Fig. 6b. Thus the presence of a peak at approximately 850 °C associated to the reduction of Cu(II) [116] supports the assignation of the high temperature reduction peak for copper samples. Clearly, the reduction of Cu(II) species take place at lower temperatures in the Cu-PZ and Cu-PZC samples than in CuO reference, revealing, once again, the interaction between the support and the CuO phase, as it was previously observed in the H₂-TPR profiles. Finally, due to the presence of the CuO phase on the surface of the pyrochlore supports, the impregnated samples evolve a much higher amount of oxygen than the raw samples, which could be relevant for the catalytic reaction under study.

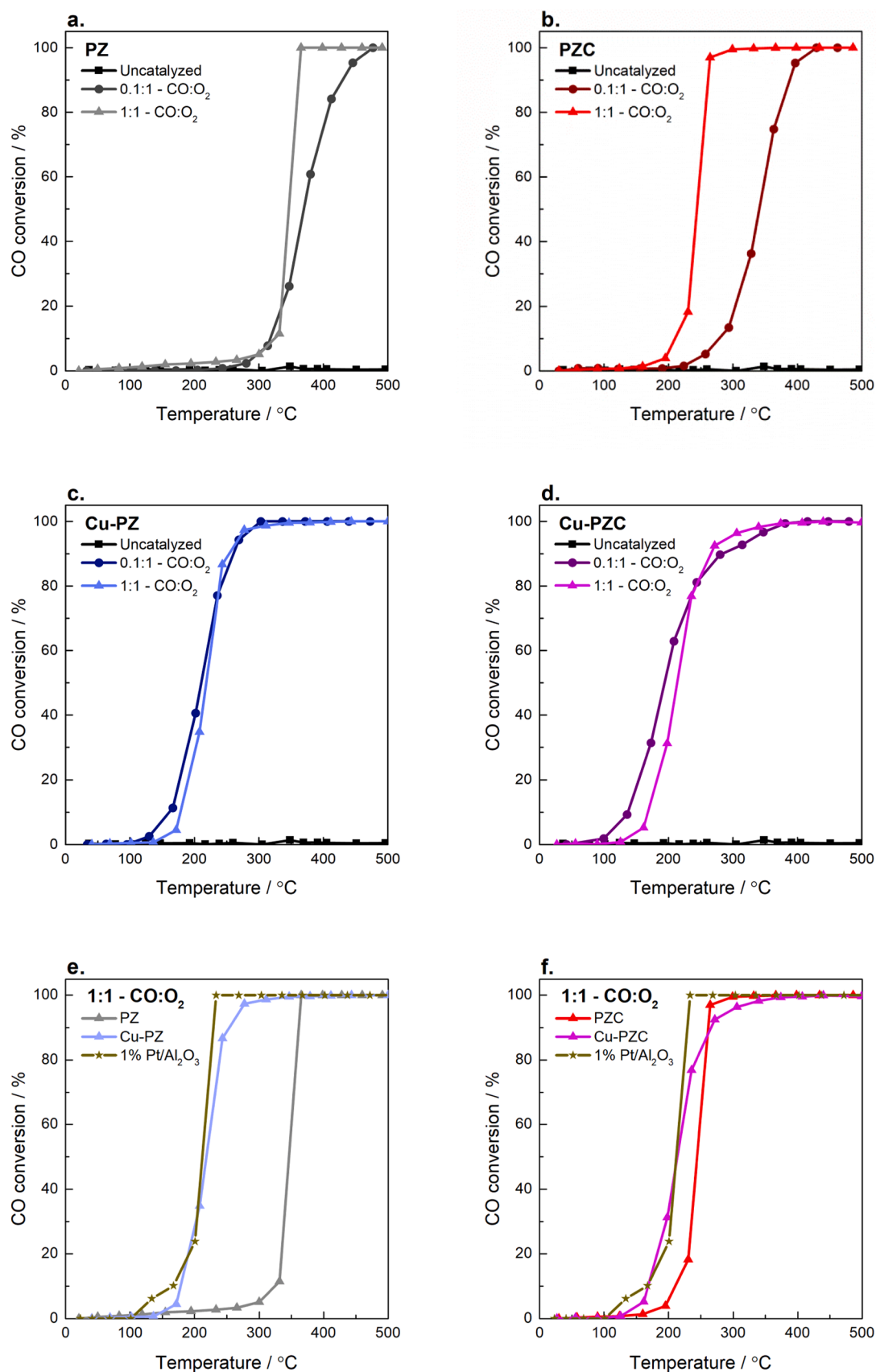


Fig. 7. CO-TPR conversion profiles for (a) PZ, (b) PZC, (c) Cu-PZ, and (d) Cu-PZC in 0.1% CO/1% O₂ and 1% CO/1% O₂ gas mixtures. (e and f) Comparison of Cu impregnated and non-impregnated samples in 1% CO/1% O₂ gas mixtures. The CO-TPR profile of a 1% Pt/Al₂O₃ reference sample is included for comparative purposes.

Table 4T_{50%} values (°C) for samples in the two reactant mixtures tested.

Sample	0.1% CO, 1% O ₂	1% CO, 1% O ₂
PZ	370	346
PZC	341	244
Cu-PZ	210	218
Cu-PZC	194	213
1% Pt/Al ₂ O ₃	163	212

3.4. Catalytic activity

The CO-TPR profiles of the four samples are shown in Fig. 7 for the two tested reaction gas mixtures. All the samples catalyze CO oxidation since the uncatalyzed reaction does not occur at temperatures below 500 °C. From these profiles, the temperature at which the 50% of CO conversion is achieved, called T_{50%}, has been obtained, being the data included in Table 3. T_{50%} values for PZ and PZC samples reveal that the catalysts are more effective if a higher CO concentration is present in the reaction mixture, so, it seems that under the same partial pressure of CO and O₂, the catalysts promote the CO oxidation to CO₂ at lower temperatures. However, note that the decrease in the T_{50%} value for PZC is almost of 100 °C, being much larger than the observed for the PZ sample (only of 24 °C). The highest CO conversion detected for PZC reveals the well-known catalytic role of Ce in the CO oxidation reaction [117–119].

On the other hand, as it could be expected for copper-containing samples, the CO oxidation reaction takes place at lower temperatures than for raw samples. Additionally, as it was also observed for copper-supported perovskites [53], the difference between the T_{50%} values in the two tested gas mixtures are not significant (Table 4). This result suggests that copper provides additional active sites for the reaction [120–123]. The electronic configuration of Cu(II) ions, with unpaired valence electrons in *d* orbitals, enables the activation of CO molecules and modifies the active site geometry of the support surface, enhancing CO conversion [33,35,55]. Briefly, CO molecules are initially adsorbed onto the CuO surface through weak Van der Waals interactions. Subsequently, CO molecules undergo activation (typically through the interaction with Cu or oxygen vacancies on the CuO surface). The activation implies that the σ bond of CO molecule is partially broken, by the formation of chemisorbed species, M_x(CO)_y, because the electrons of Cu are transferred to vacant anti-bonding π^* -orbitals of CO. These surface chemisorbed species improve the selective oxidation of CO to form CO₂ [124,125].

Note that, as observed for raw samples, the presence of Ce in the

composition of pyrochlore increases the CO conversion, being T_{50%} values for Cu-PZC lower than for Cu-PZ. The better performance of the Cu-PZC sample is probably due to an increase in the number of defects and oxygen vacancies in the pyrochlore bulk (as revealed by the higher amount of O₂ evolved, observed in Fig. 6b), which facilitate the ionic mobility and the adsorption of gas. These samples present a better performance than the observed when a barium deficient perovskite (Ba_{0.7}MnO₃) is used as support for the same amount of copper, that shows a T_{50%} around 253 °C in both gas mixtures [53].

Additionally, a significant factor influencing the catalytic activity is the bond dissociation energy. In the case of the PZ and PZC samples, the dissociation energies are similar, with the Zr-O, Pr-O, and Ce-O bonds presenting energies of 760 kJ mol⁻¹, 753 kJ mol⁻¹, and 795 kJ mol⁻¹ at 298 K, respectively. Conversely, for the Cu-impregnated samples, the Cu-O energy is considerably lower, 343 kJ mol⁻¹ [126–129], justifying that copper-impregnated samples present a higher catalytic activity than raw samples.

To show more clearly the effect of copper, the CO-TPR profiles obtained for the raw and the copper impregnated samples in the 1:1 gas mixture have been compared in Fig. 7e for PZ, and in Fig. 7f for PZC. It is observed that the CO conversion is noticeably increased by copper only for the PZ sample and that, in the presence of Ce, a more similar CO conversion profiles are detected for PZC and Cu-PZC.

The CO-TPR profiles of a 1% Pt/Al₂O₃ commercial sample, used as reference [130], have been included in Figs. 7e and 7f for comparative purposes. It has to be underlined that the Cu-impregnated samples exhibit T_{50%} values similar to those of the reference catalyst (see data in Table 4), particularly for the near stoichiometric gas mixture. So, this finding highlights the potential of these materials as promising catalysts for the CO oxidation reaction.

As the Cu-impregnated samples have shown more promising results, stability tests consisting in two consecutive reactions at 300 °C (3 h each cycle) were conducted. These tests are shown in Figs. 8a and 8b for the Cu-PZ and Cu-PZC samples, respectively. Both samples present not only a high stability over the 3 h reaction time, as CO conversions between 75% and 85% are observed, but also a high recyclability as they exhibited similar CO conversions during the second cycle (in red).

Considering the analyzed CO conversion data, a reaction pathway based on the mechanisms proposed in the literature can be suggested [131]. The CO oxidation reaction needs the adsorption of O₂ molecules on the surface of the solid to generate reactive oxygen species, ROS (Eq. 5), following a Langmuir-Hinshelwood mechanism, which also involves CO adsorption on the catalysts surface, as previously described. This

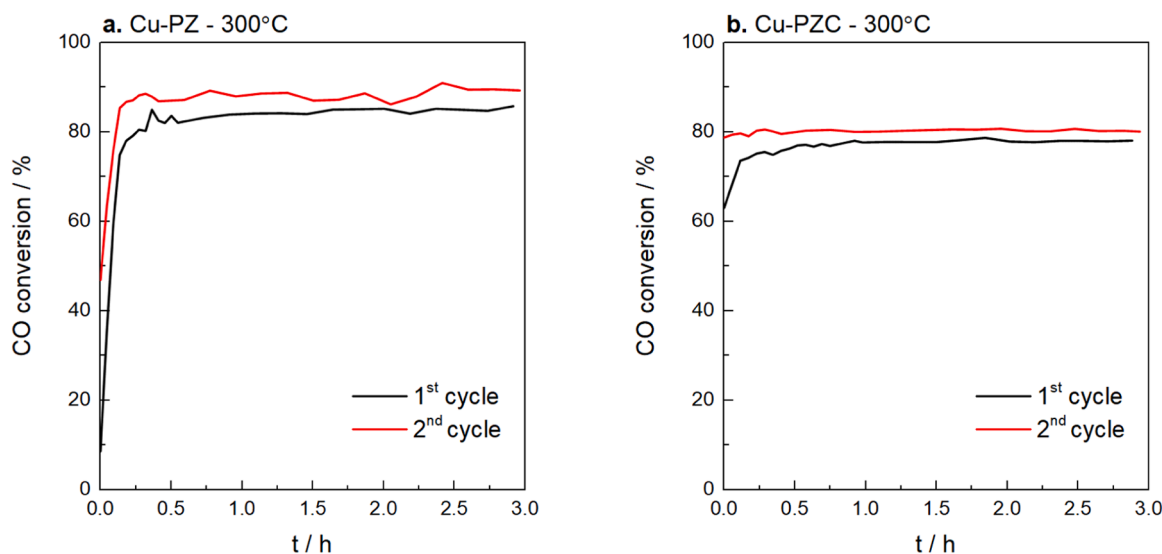
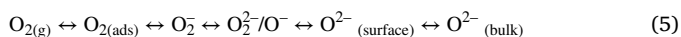


Fig. 8. Long-term stability test for CO oxidation at 300 °C of: (a) Cu-PZ and (b) Cu-PZC samples.

mechanism suggests that the rate of the reaction is proportional to the concentration of the adsorbed reactants on the catalyst surface, where the formation of intermediate species occurs.



For ROS generation, electrons are necessary for reducing the O_2 molecules adsorbed on the surface, and it seems that there are two possible sources of electrons. The first one is based on the direct electron transfer from the support surface, which comes from Pr and Ce, as they have electron donor properties. The second mechanism involves the regeneration of ROS by CO molecules adsorbed. The lower $T_{50\%}$ values observed in the 1:1 $\text{CO}:\text{O}_2$ gas mixture could be attributed to the increased interaction of CO with the oxygen species adsorbed on the surface, leading to electron transfer and a lower activation energy required for ROS generation, compared to the 0.1:1 $\text{CO}:\text{O}_2$ gas mixture. Additionally, at temperatures higher than the corresponding to reduction of the Pr(IV) (and Ce(IV)) species to Pr(III) (and Ce(III)) (see the H_2 -TPR profiles), a Mars-van Krevelen (MvK) mechanism could also contribute, involving the oxygen released from the catalyst surface. Finally, the lattice oxygen consumed during the reaction could be regenerated through the adsorption of oxygen from the gas phase, its dissociation, and its incorporation in the lattice [82].

In summary, the results discussed above indicate that pyrochlores show interesting catalytic properties as catalysts and/or catalyst supports for copper, and that the incorporation of Ce into the pyrochlore composition leads to a high catalytic activity even in the absence of copper. Additionally, the impregnation of the samples with Cu enhances their redox properties, thus improving their catalytic activity and, consequently, making them a promising alternative to the use of noble metal-based catalyst.

4. Conclusions

In this study, the catalytic activity of $\text{Pr}_2\text{Zr}_2\text{O}_7$ (PZ) and $\text{Pr}_2\text{Zr}_{1.9}\text{Ce}_{0.1}\text{O}_{7\pm\delta}$ (PZC) and the corresponding copper impregnated samples (Cu-PZ and Cu-PZC) for the CO oxidation reaction in simulated GDI engine conditions has been determined and based on the characterization data and catalytic activity tests, the following conclusions can be drawn:

- (1) Solvothermal method allows the synthesis of single-phase pyrochlore structures (PZ and PZC), as evidenced by the XRD data. No significant difference in particle size between samples is detected by FE-SEM, being the surface area slightly lower upon cerium incorporation into the structure.
- (2) XPS data revealed the presence of Pr(III) and Pr(IV) oxidation states for all compositions. Ce(III) and Ce(IV) species should be also present on the surface for PZC and Cu-PZC samples.
- (3) Copper was successfully incorporated onto the samples by the incipient wetness impregnation method, as the XRD and HR-TEM analysis reveal the presence of CuO phase. The Cu impregnation led to a decrease in the specific surface area, probably due to the sintering during the calcination step after impregnation. Redox properties, evaluated by H_2 -TPR and O_2 -TPD profiles, have been also significantly enhanced by copper.
- (4) Cu-TPR experiments demonstrated that the raw samples exhibited a better catalytic performance in the near stoichiometric gas mixture (1% CO and 1% O_2), while Cu-impregnated samples showed a similar performance in both tested gas mixtures. Cu-PZC presents a slightly better performance than Cu-PZ, showing a CO conversion in the near stoichiometric gas mixture (1% CO, 1% O_2) similar to the 1% Pt/ Al_2O_3 reference sample. Additionally, both copper samples exhibited a high stability during two consecutive isothermal tests conducted at 300 °C.

These results allow to conclude that pyrochlores present promising properties as catalysts and/or catalyst supports. Furthermore, the use of Cu supported on pyrochlores seems to be an efficient and cost-effective alternative to noble metal-based catalysts involved in the control of the composition of exhaust gas combustion engines.

CRediT authorship contribution statement

E. L. S: V: Conceptualization, Methodology, Validation, Formal analysis, Investigation, Visualization, Writing – original draft. **Á. D-V:** Conceptualization, Methodology, Validation, Formal analysis, Investigation, Visualization, Writing – review & editing. **M.J. I-G:** Conceptualization, Methodology, Resources, Writing – review & editing. **H B-M:** Conceptualization, Methodology, Resources, Supervision Writing – review & editing. **E C:** Conceptualization, Methodology, Resources, Supervision, Writing – review & editing.

Declaration of Competing Interest

The authors declare that they have no known competing financial interests or personal relationships that could have appeared to influence the work reported in this paper.

Data Availability

Data will be made available on request.

Acknowledgments

H.B-M, E.C. and E.L.S.V. thank the Spanish Government (Ministerio de Ciencia e Innovación, Project PID2020-116149GB-I00) for the financial support. E.L.S.V thanks the Generalitat Valenciana for the predoctoral contract (GRISOLIA/2019/054). A.D-V and M.J.I-G thank the Spanish Government (Ministerio de Ciencia e Innovación, Project PID2019-105542RB-I00), the European Union (FEDER Funds) and the Regional Government (Generalitat Valenciana, Project CIPROM/2021-070) for the financial support. A.D-V thanks the University of Alicante for the financial support for the predoctoral contract.

Appendix A. Supporting information

Supplementary data associated with this article can be found in the online version at [doi:10.1016/j.apcatb.2023.123371](https://doi.org/10.1016/j.apcatb.2023.123371).

References

- [1] T. Capurso, M. Stefanizzi, M. Torresi, S.M. Camporeale, Perspective of the role of hydrogen in the 21st century energy transition, *Energy Convers. Manag.* 251 (2022), 114898, <https://doi.org/10.1016/j.enconman.2021.114898>.
- [2] E.B. Agyekum, C. Nutakor, A.M. Agwa, S. Kamel, A critical review of renewable hydrogen production methods: factors affecting their scale-up and its role in future energy generation, *Membr. (Basel)* 12 (2022) 173, <https://doi.org/10.3390/membranes12020173>.
- [3] D. Balsalobre-Lorente, A. Álvarez-Herranz, M. Shahbaz, The long-term effect of economic growth, energy innovation, energy use on environmental quality, in: *Energy and Environmental Strategies in the Era of Globalization*, 1st ed., Springer, Cham, Switzerland, 2019, pp. 1–34, https://doi.org/10.1007/978-3-030-06001-5_1.
- [4] Y. Huang, N.C. Surawski, B. Organ, J.L. Zhou, O.H.H. Tang, E.F.C. Chan, Fuel consumption and emissions performance under real driving: comparison between hybrid and conventional vehicles, *Sci. Total Environ.* 659 (2019) 275–282, <https://doi.org/10.1016/j.scitotenv.2018.12.349>.
- [5] C. Oberschelp, S. Pfister, C.E. Raptis, S. Hellweg, Global emission hotspots of coal power generation, *Nat. Sustain.* 2 (2019) 113–121, <https://doi.org/10.1038/s41893-019-0221-6>.
- [6] J. Zhang, Q. Zhang, X. Feng, Support and interface effects in water-splitting electrocatalysts, *Adv. Mater.* 31 (2019), 1808167, <https://doi.org/10.1002/adma.201808167>.
- [7] T. Zheng, K. Jiang, N. Ta, Y. Hu, J. Zeng, J. Liu, H. Wang, Large-scale and highly selective CO_2 electrocatalytic reduction on nickel single-atom catalyst, *Joule* 3 (2019) 265–278, <https://doi.org/10.1016/j.joule.2018.10.015>.

- [8] D.M. Weekes, D.A. Salvatore, A. Reyes, A. Huang, C.P. Berlinguette, Electrolytic CO₂ reduction in a flow cell, *Acc. Chem. Res.* 51 (2018) 910–918, <https://doi.org/10.1021/acs.accounts.8b00010>.
- [9] Z. Pan, Y. Liu, A. Tahir, O. Christopher Esan, J. Zhu, R. Chen, L. An, A discrete regenerative fuel cell mediated by ammonia for renewable energy conversion and storage, *Appl. Energy* 322 (2022), 119463, <https://doi.org/10.1016/j.apenergy.2022.119463>.
- [10] A.C. Bhosale, P.C. Ghosh, L. Assaud, Preparation methods of membrane electrode assemblies for proton exchange membrane fuel cells and unitized regenerative fuel cells: a review, *Renew. Sustain. Energy Rev.* 133 (2020), 110286, <https://doi.org/10.1016/j.rser.2020.110286>.
- [11] Z. Pu, G. Zhang, A. Hassanpour, D. Zheng, S. Wang, S. Liao, Z. Chen, S. Sun, Regenerative fuel cells: recent progress, challenges, perspectives and their applications for space energy system, *Appl. Energy* 283 (2021), 116376, <https://doi.org/10.1016/j.apenergy.2020.116376>.
- [12] J. Adánez, A. Abad, T. Mendiara, P. Gayán, L.F. de Diego, F. García-Labiano, Chemical looping combustion of solid fuels, *Prog. Energy Combust. Sci.* 65 (2018) 6–66, <https://doi.org/10.1016/j.pecs.2017.07.005>.
- [13] Y. Demirel, M. Matzen, C. Winters, G. Gao, Capturing and using CO₂ as feedstock with chemical looping and hydrothermal technologies, *Int. J. Energy Res.* 39 (2015) 1011–1047, <https://doi.org/10.1002/er.3277>.
- [14] L.-S. Fan, F. Li, Chemical looping technology and its fossil energy conversion applications, *Ind. Eng. Chem. Res.* 49 (2010) 10200–10211, <https://doi.org/10.1021/ie100554z>.
- [15] D. Xu, A. Tong, L.-S. Fan, State of scale-up development in chemical looping technology for biomass conversions: a review and perspectives, *Waste Biomass Valoriz.* 13 (2022) 1363–1383, <https://doi.org/10.1007/s12649-021-01563-2>.
- [16] J. Hou, M. Yang, J. Zhang, Recent advances in catalysts, electrolytes and electrode engineering for the nitrogen reduction reaction under ambient conditions, *Nanoscale* 12 (2020) 6900–6920, <https://doi.org/10.1039/D0NR00412J>.
- [17] Z. Jiang, C. Xia, F. Chen, Nano-structured composite cathodes for intermediate-temperature solid oxide fuel cells via an infiltration/impregnation technique, *Electro Acta* 55 (2010) 3595–3605, <https://doi.org/10.1016/j.electacta.2010.02.019>.
- [18] M. Zhang, G. Jeerh, P. Zou, R. Lan, M. Wang, H. Wang, S. Tao, Recent development of perovskite oxide-based electrocatalysts and their applications in low to intermediate temperature electrochemical devices, *Mater. Today* 49 (2021) 351–377, <https://doi.org/10.1016/j.mattod.2021.05.004>.
- [19] X. Liu, K. Reddi, A. Elgowainy, H. Lohse-Busch, M. Wang, N. Rustagi, Comparison of well-to-wheels energy use and emissions of a hydrogen fuel cell electric vehicle relative to a conventional gasoline-powered internal combustion engine vehicle, *Int. J. Hydrog. Energy* 45 (2020) 972–983, <https://doi.org/10.1016/j.ijhydene.2019.10.192>.
- [20] Y. Huang, N.C. Surawski, B. Organ, J.L. Zhou, O.H.H. Tang, E.F.C. Chan, Fuel consumption and emissions performance under real driving: Comparison between hybrid and conventional vehicles, *Sci. Total Environ.* 659 (2019) 275–282, <https://doi.org/10.1016/j.scitotenv.2018.12.349>.
- [21] F. Leach, G. Kalghatgi, R. Stone, P. Miles, The scope for improving the efficiency and environmental impact of internal combustion engines, *Transp. Eng.* 1 (2020), 100005, <https://doi.org/10.1016/j.treng.2020.100005>.
- [22] S. Rood, S. Eslava, A. Manigrasso, C. Bannister, Recent advances in gasoline three-way catalyst formulation: A review, *Proc. Inst. Mech. Eng., Part D: J. Automob. Eng.* 234 (2020) 936–949, <https://doi.org/10.1177/0954407019859822>.
- [23] J. Wang, H. Chen, Z. Hu, M. Yao, Y. Li, A Review on the Pd-Based Three-Way Catalyst, *Catal. Rev.* 57 (2015) 79–144, <https://doi.org/10.1080/01614940.2014.977059>.
- [24] J.R. Theis, A. Getsoian, C. Lambert, The Development of Low Temperature Three-Way Catalysts for High Efficiency Gasoline Engines of the Future, 2017-01-0918, *SAE Int. J. Fuels Lubr.* 10 (2017), <https://doi.org/10.4271/2017-01-0918>.
- [25] Q. Zuo, T. Liu, C. Chen, Y. Ji, X. Gong, Y. Mai, Y. Zhou, Ultrathin metal-organic framework nanosheets with ultrahigh loading of single Pt atoms for efficient visible-light-driven photocatalytic H₂ evolution, *Angew. Chem. Int. Ed.* 58 (2019) 10198–10203, <https://doi.org/10.1002/anie.201904058>.
- [26] L. Zhang, K. Doyle-Davis, X. Sun, Pt-Based electrocatalysts with high atom utilization efficiency: from nanostructures to single atoms, *Energy Environ. Sci.* 12 (2019) 492–517, <https://doi.org/10.1039/C8EE02939C>.
- [27] K. Jiang, B. Liu, M. Luo, S. Ning, M. Peng, Y. Zhao, Y.-R. Lu, T.-S. Chan, F.M.F. de Groot, Y. Tan, Single platinum atoms embedded in nanoporous cobalt selenide as electrocatalyst for accelerating hydrogen evolution reaction, *Nat. Commun.* 10 (2019) 1743, <https://doi.org/10.1038/s41467-019-09765-y>.
- [28] B. Qiao, A. Wang, X. Yang, L.F. Allard, Z. Jiang, Y. Cui, J. Liu, J. Li, T. Zhang, Single-atom catalysis of CO oxidation using Pt₁/FeO_x, *Nat. Chem.* 3 (2011) 634–641, <https://doi.org/10.1038/nchem.1095>.
- [29] T. Varga, G. Ballai, L. Vászárheli, H. Haspel, A. Kukovecz, Z. Kónya, Co₄N/nitrogen-doped graphene: A non-noble metal oxygen reduction electrocatalyst for alkaline fuel cells, *Appl. Catal. B* 237 (2018) 826–834, <https://doi.org/10.1016/j.apcatb.2018.06.054>.
- [30] K. Srinivasu, S.K. Ghosh, Transition Metal Decorated Graphyne: An Efficient Catalyst for Oxygen Reduction Reaction, *J. Phys. Chem. C* 117 (2013) 26021–26028, <https://doi.org/10.1021/jp407007n>.
- [31] T. Asset, P. Atanassov, Iron-Nitrogen-Carbon Catalysts for Proton Exchange Membrane Fuel Cells, *Joule* 4 (2020) 33–44, <https://doi.org/10.1016/j.joule.2019.12.002>.
- [32] T.K. Todorova, M.W. Schreiber, M. Fontecave, Mechanistic Understanding of CO₂ Reduction Reaction (CO₂RR) Toward Multicarbon Products by Heterogeneous Copper-Based Catalysts, *ACS Catal.* 10 (2020) 1754–1768, <https://doi.org/10.1021/acscatal.9b04746>.
- [33] A. Vasileff, C. Xu, Y. Jiao, Y. Zheng, S.-Z. Qiao, Surface and Interface Engineering in Copper-Based Bimetallic Materials for Selective CO₂ Electroreduction, *Chem* 4 (2018) 1809–1831, <https://doi.org/10.1016/j.chempr.2018.05.001>.
- [34] Y. Zheng, A. Vasileff, X. Zhou, Y. Jiao, M. Jaroniec, S.-Z. Qiao, Understanding the roadmap for electrochemical reduction of CO₂ to multi-carbon oxygenates and hydrocarbons on copper-based catalysts, *J. Am. Chem. Soc.* 141 (2019) 7646–7659, <https://doi.org/10.1021/jacs.9b02124>.
- [35] J. Papavasiliou, G. Slowik, G. Avgouropoulos, Redox behavior of a copper-based methanol reformer for fuel cell applications, *Energy Technol.* 6 (2018) 1332–1341, <https://doi.org/10.1002/ente.201700883>.
- [36] R. Ye, S. Xiao, Q. Lai, D. Wang, Y. Huang, G. Feng, R. Zhang, T. Wang, Advances in enhancing the stability of Cu-based catalysts for methanol reforming, *Catalysts* 12 (2022) 747, <https://doi.org/10.3390/catal12070747>.
- [37] C. Yang, G. Miao, Y. Pi, Q. Xia, J. Wu, Z. Li, J. Xiao, Abatement of various types of VOCs by adsorption/catalytic oxidation: a review, *Chem. Eng. J.* 370 (2019) 1128–1153, <https://doi.org/10.1016/j.cej.2019.03.232>.
- [38] S. Dey, G. Chandra Dhal, Controlling carbon monoxide emissions from automobile fuel exhaust using copper oxide catalysts in a catalytic converter, *Mater. Today Chem.* 17 (2020), 100282, <https://doi.org/10.1016/j.mtchem.2020.100282>.
- [39] S. Dey, G.C. Dhal, A review of synthesis, structure and applications in hopcalite catalysts for carbon monoxide oxidation, *Aerosol Sci. Eng.* 3 (2019) 97–131, <https://doi.org/10.1007/s41810-019-00046-1>.
- [40] G.G. Jernigan, G.A. Somorjai, Carbon monoxide oxidation over three different oxidation states of copper: metallic copper, copper (I) oxide, and copper (II) oxide - a surface science and kinetic study, *J. Catal.* 147 (1994) 567–577, <https://doi.org/10.1006/jcat.1994.1173>.
- [41] Z. Shen, X. Xing, S. Wang, M. Lv, Z. Zheng, J. Li, H. Li, High activity of CuO/ γ -Fe₂O₃ for low temperature CO oxidation: effect of support crystal types in catalyst design, *J. Energy Inst.* 110 (2023), <https://doi.org/10.1016/j.joei.2023.101339>.
- [42] Z. Zhang, L. Fan, W. Liao, F. Zhao, C. Tang, J. Zhang, M. Feng, J.-Q. Lu, Structure sensitivity of CuO in CO oxidation over CeO₂-CuO/Cu₂O catalysts, *J. Catal.* 405 (2022) 333–345, <https://doi.org/10.1016/j.jcat.2021.12.015>.
- [43] S. Dey, G.C. Dhal, D. Mohan, R. Prasad, Structural and catalytic properties of Fe and Ni doping on CuMnO_x catalyst for CO oxidation, *Adv. Compos. Hybrid. Mater.* 3 (2020) 84–97, <https://doi.org/10.1007/s42114-020-00139-3>.
- [44] S. Dey, G.C. Dhal, D. Mohan, R. Prasad, The choice of precursors in the synthesizing of CuMnO_x catalysts for maximizing CO oxidation, *Int. J. Ind. Chem.* 9 (2018) 199–214, <https://doi.org/10.1007/s40090-018-0150-7>.
- [45] S. Dey, G. Chandra Dhal, D. Mohan, R. Prasad, Synthesis of silver promoted CuMnO_x catalyst for ambient temperature oxidation of carbon monoxide, *J. Sci.: Adv. Mater. Devices* 4 (2019) 47–56, <https://doi.org/10.1016/j.jsamd.2019.01.008>.
- [46] S. Dey, G.C. Dhal, D. Mohan, R. Prasad, R.N. Gupta, Cobalt doped CuMnO_x catalysts for the preferential oxidation of carbon monoxide, *Appl. Surf. Sci.* 441 (2018) 303–316, <https://doi.org/10.1016/j.apsusc.2018.02.048>.
- [47] R. Prasad, P. Singh, A review on CO oxidation over copper chromite catalyst, *Catal. Rev.* 54 (2012) 224–279, <https://doi.org/10.1080/01614940.2012.648494>.
- [48] P.K. Gallagher, D.W. Johnson, E.M. Vogel, Preparation, structure, and selected catalytic properties of the system LaMn_{1-x}Cu_xO_{3-y}, *J. Am. Ceram. Soc.* 60 (1977) 28–31, <https://doi.org/10.1111/j.1151-2916.1977.tb16086.x>.
- [49] K.S. Chan, J. Ma, S. Jaenicke, G.K. Chuah, J.Y. Lee, Catalytic carbon monoxide oxidation over strontium, cerium and copper-substituted lanthanum manganates and cobaltates, *Appl. Catal. A Gen.* 107 (1994) 201–227, [https://doi.org/10.1016/0926-860X\(94\)85156-5](https://doi.org/10.1016/0926-860X(94)85156-5).
- [50] S. Royer, F. Bérubé, S. Kaliaguine, Effect of the synthesis conditions on the redox and catalytic properties in oxidation reactions of LaCo_{1-x}Fe_xO₃, *Appl. Catal. A Gen.* 282 (2005) 273–284, <https://doi.org/10.1016/j.apcata.2004.12.018>.
- [51] N. Yamazoe, Y. Teraoka, Oxidation catalysis of perovskites - relationships to bulk structure and composition (valency, defect, etc.), *Catal. Today* 8 (1990) 175–199, [https://doi.org/10.1016/0926-860X\(90\)87017-W](https://doi.org/10.1016/0926-860X(90)87017-W).
- [52] D. Pinto, A. Glisenti, Pulsed reactivity on LaCoO₃-based perovskites: a comprehensive approach to elucidate the CO oxidation mechanism and the effect of dopants, *Catal. Sci. Technol.* 9 (2019) 2749–2757, <https://doi.org/10.1039/C9CY00210C>.
- [53] A. Díaz-Verde, V. Torregrosa-Rivero, M.J. Illán-Gómez, Copper catalysts supported on barium deficient perovskites for CO oxidation reaction, *Top. Catal.* (2022), <https://doi.org/10.1007/s12444-022-01716-0>.
- [54] W. Zhan, Y. Guo, X. Gong, Y. Guo, Y. Wang, G. Lu, Current status and perspectives of rare earth catalytic materials and catalysis, *Chin. J. Catal.* 35 (2014) 1238–1250, [https://doi.org/10.1016/S1872-2067\(14\)60189-3](https://doi.org/10.1016/S1872-2067(14)60189-3).
- [55] L. Wu, Y. Hao, S. Chen, R. Chen, P. Sun, T. Chen, Effects of rare earth metal doping on Au/ReZrO₂ catalysts for efficient hydrogen generation from formic acid, *N. J. Chem.* 45 (2021) 5704–5711, <https://doi.org/10.1039/D0NJ06124G>.
- [56] M. Pudukudy, Z. Yaakob, Q. Jia, M.S. Takriff, Catalytic decomposition of methane over rare earth metal (Ce and La) oxides supported iron catalysts, *Appl. Surf. Sci.* 468 (2019) 236–248, <https://doi.org/10.1016/j.apsusc.2018.10.122>.
- [57] W. Li, S. Wang, J. Li, Effect of rare earth elements (La, Y, Pr) in multi-element composite perovskite oxide supports for ammonia synthesis, *J. Rare Earths* 39 (2021) 427–433, <https://doi.org/10.1016/j.jre.2020.06.006>.
- [58] W. She, T. Qi, M. Cui, P. Yan, S.W. Ng, W. Li, G. Li, High catalytic performance of a CeO₂-supported Ni catalyst for hydrogenation of nitroarenes, fabricated via

- coordination-assisted strategy, *ACS Appl. Mater. Interfaces* 10 (2018) 14698–14707, <https://doi.org/10.1021/acsami.8b01187>.
- [59] A.Q.M. Boon, H.M. Huisman, J.W. Geus, Influence of surface oxygen vacancies on the catalytic activity of copper oxide Part 2. Oxidation of methane, *J. Mol. Catal.* 75 (1992) 293–303, [https://doi.org/10.1016/0304-5102\(92\)80132-Z](https://doi.org/10.1016/0304-5102(92)80132-Z).
- [60] S. Royer, D. Duprez, Catalytic oxidation of carbon monoxide over transition metal oxides, *ChemCatChem* 3 (2011) 24–65, <https://doi.org/10.1002/cctc.201000378>.
- [61] J. Shi, H. Li, W. Zhao, P. Qi, H. Wang, Praseodymium hydroxide/gold-supported precursor: a new strategy for preparing stable and active catalyst for the water-gas shift reaction, *Catal. Sci. Technol.* 10 (2020) 7291–7301, <https://doi.org/10.1039/D0CY01263G>.
- [62] S. Carabineiro, M. Konsolakis, G. Marnellos, M. Asad, O. Soares, P. Tavares, M. Pereira, J. Órfão, J. Figueiredo, Ethyl acetate abatement on copper catalysts supported on ceria doped with rare earth oxides, *Molecules* 21 (2016) 644, <https://doi.org/10.3390/molecules21050644>.
- [63] X. Fang, J. Zhang, J. Liu, C. Wang, Q. Huang, X. Xu, H. Peng, W. Liu, X. Wang, W. Zhou, Methane dry reforming over Ni/Mg-Al-O: On the significant promotional effects of rare earth Ce and Nd metal oxides, *J. CO₂ Util.* 25 (2018) 242–253, <https://doi.org/10.1016/j.jcou.2018.04.011>.
- [64] H. Liu, B. Zhao, Y. Chen, C. Ren, Y. Chen, Rare earths (Ce, Y, Pr) modified Pd/La₂O₃-ZrO₂-Al₂O₃ catalysts used in lean-burn natural gas fueled vehicles, *J. Rare Earths* 35 (2017) 1077–1082, <https://doi.org/10.1016/j.jre.2017.07.006>.
- [65] V.R. Choudhary, B. Prabhakar, A.M. Rajput, A.S. Mamman, Oxidative conversion of methane to CO and H₂ over Pt or Pd containing alkaline and rare earth oxide catalysts, *Fuel* 77 (1998) 1477–1481, [https://doi.org/10.1016/S0016-2361\(98\)00063-5](https://doi.org/10.1016/S0016-2361(98)00063-5).
- [66] M. Kim, J. Park, M. Kang, J.Y. Kim, S.W. Lee, Toward efficient electrocatalytic oxygen evolution: emerging opportunities with metallic pyrochlore oxides for electrocatalysts and conductive supports, *ACS Cent. Sci.* 6 (2020) 880–891, <https://doi.org/10.1021/acscentsci.0c00479>.
- [67] X. Feng, R. Liu, X. Xu, Y. Tong, S. Zhang, J. He, J. Xu, X. Fang, X. Wang, Stable CuO/La₂Sn₂O₇ catalysts for soot combustion: Study on the monolayer dispersion behavior of CuO over a La₂Sn₂O₇ pyrochlore support, *Chin. J. Catal.* 42 (2021) 396–408, [https://doi.org/10.1016/S1872-2067\(20\)63657-9](https://doi.org/10.1016/S1872-2067(20)63657-9).
- [68] J. Deng, S. Li, X. Yin, M. Li, J. Wang, Y. Chen, Y. Chen, Influence of surface Ce/Zr ratio on formation of κ -Ce₂Zr₂O₈ superstructure and its application in three-way catalysis, *J. Rare Earths* 41 (2023) 67–76, <https://doi.org/10.1016/j.jre.2021.12.005>.
- [69] M. Kim, J. Park, H. Ju, J.Y. Kim, H.-S. Cho, C.-H. Kim, B.-H. Kim, S.W. Lee, Understanding synergistic metal–oxide interactions of in situ exsolved metal nanoparticles on a pyrochlore oxide support for enhanced water splitting, *Energy Environ. Sci.* 14 (2021) 3053–3063, <https://doi.org/10.1039/D0EE02935A>.
- [70] R.R. Jitta, R. Gundeboina, N.K. Veldurthi, R. Guje, V. Muga, Defect pyrochlore oxides: as photocatalyst materials for environmental and energy applications - a review, *J. Chem. Technol. Biotechnol.* 90 (2015) 1937–1948, <https://doi.org/10.1002/jctb.4745>.
- [71] J. Xu, R. Xi, X. Xu, Y. Zhang, X. Feng, X. Fang, X. Wang, A₂B₂O₇ pyrochlore compounds: a category of potential materials for clean energy and environment protection catalysis, *J. Rare Earths* 38 (2020) 840–849, <https://doi.org/10.1016/j.jre.2020.01.002>.
- [72] A.P. Anantharaman, H.P. Dasari, Potential of pyrochlore structure materials in solid oxide fuel cell applications, *Ceram. Int* 47 (2021) 4367–4388, <https://doi.org/10.1016/j.ceramint.2020.10.012>.
- [73] G.R. Lumpkin, R.D. Aughterson, Perspectives on pyrochlores, defect fluorites, and related compounds: building blocks for chemical diversity and functionality, *Front Chem.* 9 (2021), <https://doi.org/10.3389/fchem.2021.778140>.
- [74] P. Gayen, S. Saha, V. Ramani, Pyrochlores for advanced oxygen electrocatalysis, *Acc. Chem. Res.* 55 (2022) 2191–2200, <https://doi.org/10.1021/acs.accounts.2c00049>.
- [75] P. Duan, C. Han, Y. Zheng, G. Cai, F. Zhong, Y. Xiao, A₂B₂O₇ (A = La, Pr, Nd, Sm, Gd and B = Ti, Zr, Sn) ceramics for mid-temperature NO₂ sensing and reduction, *J. Alloy. Compd.* 831 (2020), 154866, <https://doi.org/10.1016/j.jallcom.2020.154866>.
- [76] N. Han, M. Race, W. Zhang, R. Marotta, C. Zhang, A. Bokhari, J.J. Klemes, Perovskite and related oxide based electrodes for water splitting, *J. Clean. Prod.* 318 (2021), 128544, <https://doi.org/10.1016/j.jclepro.2021.128544>.
- [77] E.L. dos Santos Veiga, X.V. Villafruela, J. Llorca, H. Beltrán-Mir, E. Cordoncillo, The catalytic activity of the Pr₂Zr₂-xFe_xO_{7±δ} system for the CO oxidation reaction, *J. Am. Ceram. Soc.* (2022), <https://doi.org/10.1111/jace.18846>.
- [78] A.L. Patterson, The scherrer formula for X-ray particle size determination, *Phys. Rev.* 56 (1939) 978–982, <https://doi.org/10.1103/PhysRev.56.978>.
- [79] B. Wuensch, Connection between oxygen-ion conductivity of pyrochlore fuel-cell materials and structural change with composition and temperature, *Solid State Ion.* 129 (2000) 111–133, [https://doi.org/10.1016/S0167-2738\(99\)00320-3](https://doi.org/10.1016/S0167-2738(99)00320-3).
- [80] R.D. Shannon, Revised effective ionic radii and systematic studies of interatomic distances in halides and chalcogenides, *Acta Crystallogr. Sect. A* 32 (1976) 751–767, <https://doi.org/10.1107/S0567739476001551>.
- [81] S. Montilla-Verdú, V. Torregrosa-Rivero, A. Díaz-Verde, M.J. Illán-Gómez, BaFe_{1-x}Ni_xO₃ catalysts for NO_x-assisted diesel soot oxidation, *Top. Catal.* (2022), <https://doi.org/10.1007/s11244-022-01769-1>.
- [82] Á. Díaz-Verde, S. Montilla-Verdú, V. Torregrosa-Rivero, M.-J. Illán-Gómez, Tailoring the composition of BaB₂O₃ (B = Fe, Mn) mixed oxides as CO or soot oxidation catalysts in simulated GDI engine exhaust conditions, *Molecules* 28 (2023) 3327, <https://doi.org/10.3390/molecules28083327>.
- [83] A. Waehayee, P. Wattaisong, S. Wannapaiboon, N. Chanlek, H. Nakajima, J. Wittayakun, S. Suthirakun, T. Siritanon, Effects of different exchanging ions on the band structure and photocatalytic activity of defect pyrochlore oxide: a case study on KNbTeO₆, *Catal. Sci. Technol.* 10 (2020) 978–992, <https://doi.org/10.1039/C9CY01782H>.
- [84] D. Chen, D. He, J. Lu, L. Zhong, F. Liu, J. Liu, J. Yu, G. Wan, S. He, Y. Luo, Investigation of the role of surface lattice oxygen and bulk lattice oxygen migration of cerium-based oxygen carriers: XPS and designed H₂-TPR characterization, *Appl. Catal. B.* 218 (2017) 249–259, <https://doi.org/10.1016/j.apcatb.2017.06.053>.
- [85] W. Deng, Q. Dai, Y. Lao, B. Shi, X. Wang, Low temperature catalytic combustion of 1,2-dichlorobenzene over CeO₂-TiO₂ mixed oxide catalysts, *Appl. Catal. B.* 181 (2016) 848–861, <https://doi.org/10.1016/j.apcatb.2015.07.053>.
- [86] E.L. dos, S. Veiga, M. Fortunio-Morte, H. Beltrán-Mir, E. Cordoncillo, Effect of the oxidation states on the electrical properties of Fe-doped Pr₂Zr₂O₇ pyrochlore, *J. Mater. Res. Technol.* 16 (2022) 201–215, <https://doi.org/10.1016/j.jmrt.2021.11.146>.
- [87] A.V. Shlyakhtina, J.C.C. Abrantes, E. Gomes, A.N. Shchegolikhin, G.A. Vorobieva, K.I. Maslakov, A.V. Knotko, L.G. Shcherbakova, Effect of Pr³⁺/Pr⁴⁺ ratio on the oxygen ion transport and thermomechanical properties of the pyrochlore and fluorite phases in the ZrO₂-Pr₂O₃ system, *Int. J. Hydrog. Energy* 41 (2016) 9982–9992, <https://doi.org/10.1016/j.ijhydene.2016.02.152>.
- [88] I. Tankov, B. Pawelec, K. Arishtirova, S. Damyanova, Structure and surface properties of praseodymium modified alumina, *Appl. Surf. Sci.* 258 (2011) 278–284, <https://doi.org/10.1016/j.apusc.2011.08.046>.
- [89] A. Ślebarksi, A. Jezierski, A. Zygmunt, M. Neumann, S. Mähl, G. Borstel, The crystallographic, magnetic and electronic properties of RM₂X₂ (R = La, Ce, Pr; M = Cu, Ni; X = Sn, Sb), *J. Magn. Magn. Mater.* 159 (1996) 179–191, [https://doi.org/10.1016/0304-8853\(95\)00645-1](https://doi.org/10.1016/0304-8853(95)00645-1).
- [90] Y. Wang, L. Yu, R. Wang, Y. Wang, X. Zhang, Reactivity of carbon spheres templated Ce/LaCo_{0.5}Cu_{0.5}O₃ in the microwave induced H₂O₂ catalytic degradation of salicylic acid: Characterization, kinetic and mechanism studies, *J. Colloid Interface Sci.* 574 (2020) 74–86, <https://doi.org/10.1016/j.jcis.2020.04.042>.
- [91] E. Bêche, P. Charvin, D. Perarnau, S. Abanades, G. Flamant, Ce 3d XPS investigation of cerium oxides and mixed cerium oxide (Ce₂Ti₂O₇, *Surf. Interface Anal.* 40 (2008) 264–267, <https://doi.org/10.1002/sia.2686>.
- [92] L.-H. Chang, N. Sasirekha, Y.-W. Chen, W.-J. Wang, Preferential Oxidation of CO in H₂ Stream over Au/MnO₂-CeO₂ Catalysts, *Ind. Eng. Chem. Res.* 45 (2006) 4927–4935, <https://doi.org/10.1021/ie0514408>.
- [93] R. Wang, H. Xu, X. Liu, Q. Ge, W. Li, Role of redox couples of Rh⁰/Rh⁸⁺ and Ce⁴⁺/Ce³⁺ in CH₄/CO₂ reforming over Rh-CeO₂/Al₂O₃ catalyst, *Appl. Catal. A Gen.* 305 (2006) 204–210, <https://doi.org/10.1016/j.apcata.2006.03.021>.
- [94] V.B. Mortola, S. Damyanova, D. Zanchet, J.M.C. Bueno, Surface and structural features of Pt/CeO₂-La₂O₃-Al₂O₃ catalysts for partial oxidation and steam reforming of methane, *Appl. Catal. B.* 107 (2011) 221–236, <https://doi.org/10.1016/j.apcatb.2011.07.012>.
- [95] X. Liu, W. Yang, L. Chen, J. Jia, Synthesis of copper nanorods for non-enzymatic amperometric sensing of glucose, *Microchim. Acta* 183 (2016) 2369–2375, <https://doi.org/10.1007/s00604-016-1878-4>.
- [96] T. Ghoselahi, M.A. Vesaghi, A. Shafiekhani, A. Baghizadeh, M. Lameii, XPS study of the Cu@Cu₂O core-shell nanoparticles, *Appl. Surf. Sci.* 255 (2008) 2730–2734, <https://doi.org/10.1016/j.apusc.2008.08.110>.
- [97] L. Martin, H. Martinez, D. Poinot, B. Pecqueur, F. Le Cras, Comprehensive X-ray Photoelectron Spectroscopy Study of the Conversion Reaction Mechanism of CuO in Lithiated Thin Film Electrodes, *J. Phys. Chem. C* 117 (2013) 4421–4430, <https://doi.org/10.1021/jp3119633>.
- [98] N. Benito, M. Flores, Evidence of Mixed Oxide Formation on the Cu/SiO₂ Interface, *J. Phys. Chem. C* 121 (2017) 18771–18778, <https://doi.org/10.1021/acs.jpcc.7b06563>.
- [99] J. Giménez-Mañogil, N. Guillén-Hurtado, S. Fernández-García, X. Chen, J. Calvino-Gómez, A. García-García, Ceria-Praseodymia Mixed Oxides: Relationships Between Redox Properties and Catalytic Activities Towards NO Oxidation to NO₂ and CO-PROX Reactions, *Top. Catal.* 59 (2016) 1065–1070, <https://doi.org/10.1007/s11244-016-0591-1>.
- [100] N. Guillén-Hurtado, J. Giménez-Mañogil, J.C. Martínez-Munuera, A. Bueno-López, A. García-García, Study of Ce/Pr ratio in ceria-praseodymia catalysts for soot combustion under different atmospheres, *Appl. Catal. A Gen.* 590 (2020), 117339, <https://doi.org/10.1016/j.apcata.2019.117339>.
- [101] H. Zhao, D. Zhang, F. Wang, T. Wu, J. Gao, Modification of ferrite-manganese oxide sorbent by doping with cerium oxide, *Process Saf. Environ. Prot.* 86 (2008) 448–454, <https://doi.org/10.1016/j.psep.2008.06.002>.
- [102] Z. Yan, X. Shi, Y. Yu, H. He, Alkali resistance promotion of Ce-doped vanadium-titanic-based NH₃-SCR catalysts, *J. Environ. Sci.* 73 (2018) 155–161, <https://doi.org/10.1016/j.jes.2018.01.024>.
- [103] L. Chen, J. Li, M. Ge, Promotional Effect of Ce-doped V₂O₅-WO₃/TiO₂ with Low Vanadium Loadings for Selective Catalytic Reduction of NO_x by NH₃, *J. Phys. Chem. C* 113 (2009) 21177–21184, <https://doi.org/10.1021/jp907109e>.
- [104] A.A. Ansari, S.F. Adil, M. Alam, N. Ahmad, M.E. Assal, J.P. Labis, A. Alwarthan, Catalytic performance of the Ce-doped LaCoO₃ perovskite nanoparticles, *Sci. Rep.* 10 (2020) 15012, <https://doi.org/10.1038/s41598-020-71869-z>.
- [105] J. Zhu, Y. Zhao, D. Tang, Z. Zhao, S.A.C. Carabineiro, Aerobic selective oxidation of alcohols using La_{1-x}Ce_xCoO₃ perovskite catalysts, *J. Catal.* 340 (2016) 41–48, <https://doi.org/10.1016/j.jcat.2016.04.013>.
- [106] J. Yang, S. Hu, Y. Fang, S. Hoang, L. Li, W. Yang, Z. Liang, J. Wu, J. Hu, W. Xiao, C. Pan, Z. Luo, J. Ding, L. Zhang, Y. Guo, Oxygen Vacancy Promoted O₂

- Activation over Perovskite Oxide for Low-Temperature CO Oxidation, *ACS Catal.* 9 (2019) 9751–9763, <https://doi.org/10.1021/acscatal.9b02408>.
- [107] S. Watanabe, X. Ma, C. Song, Characterization of structural and surface properties of nanocrystalline TiO_2 - CeO_2 mixed oxides by XRD, XPS, TPR, and TPD, *J. Phys. Chem. C* 113 (2009) 14249–14257, <https://doi.org/10.1021/jp8110309>.
- [108] M. Ozawa, M. Misaki, M. Iwakawa, M. Hattori, K. Kobayashi, K. Higuchi, S. Arai, Low content Pt-doped CeO_2 and core-shell type $\text{CeO}_2/\text{ZrO}_2$ model catalysts; microstructure, TPR and three way catalytic activities, *Catal. Today* (2019) 251–258, <https://doi.org/10.1016/j.cattod.2018.08.015>.
- [109] A.N. Il'ichev, D.P. Shashkin, T.I. Khomenko, Z.T. Fattakhova, V.N. Korchak, Structure and surface properties of ZrO_2 , CeO_2 , and $\text{Zr}_{0.5}\text{Ce}_{0.5}\text{O}_2$ prepared by a microemulsion method according to X-ray diffraction, TPR, and EPR data, *Kinet. Catal.* 51 (2010) 743–753, <https://doi.org/10.1134/S0023158410050174>.
- [110] V. Frizon, J.-M. Bassat, M. Pollet, E. Durand, J. Hernandez, K. Pajot, P. Vernoux, A. Demourgues, Tuning the Pr valence state to design high oxygen mobility, redox and transport properties in the CeO_2 - ZrO_2 - PrO_x phase diagram, *J. Phys. Chem. C* 123 (2019) 6351–6362, <https://doi.org/10.1021/acs.jpcc.8b11469>.
- [111] G.W. M.Yu. Sinev, L.P. Graham, M. Haack, Shelef, Kinetic and structural studies of oxygen availability of the mixed oxides $\text{Pr}_{1-x}\text{M}_x\text{O}_y$ ($\text{M} = \text{Ce}, \text{Zr}$), *J. Mater. Res* 11 (1996) 1960–1971, <https://doi.org/10.1557/JMR.1996.0247>.
- [112] H. Yen, F. Kleitz, High-performance solid catalysts for H_2 generation from ammonia borane: progress through synergetic Cu–Ni interactions, *J. Mater. Chem. A Mater.* 1 (2013) 14790, <https://doi.org/10.1039/c3ta13681g>.
- [113] A.V. Fedorov, R.G. Kukushkin, P.M. Yeletsy, O.A. Bulavchenko, Y.A. Chesalov, V. A. Yakovlev, Temperature-programmed reduction of model CuO, NiO and mixed CuO–NiO catalysts with hydrogen, *J. Alloy. Compd.* 844 (2020), 156135, <https://doi.org/10.1016/j.jallcom.2020.156135>.
- [114] V. Torregrosa-Rivero, M.-S. Sánchez-Adsuar, M.-J. Illán-Gómez, Exploring the effect of using carbon black in the sol-gel synthesis of BaMnO_3 and $\text{BaMn}_{0.7}\text{Cu}_{0.3}\text{O}_3$ perovskite catalysts for CO oxidation, *Catal. Today* (2023), 114028, <https://doi.org/10.1016/j.cattod.2023.02.005>.
- [115] B. Wang, C. Chi, M. Xu, C. Wang, D. Meng, Plasma-catalytic removal of toluene over CeO_2 - MnO_x catalysts in an atmosphere dielectric barrier discharge, *Chem. Eng. J.* 322 (2017) 679–692, <https://doi.org/10.1016/j.cej.2017.03.153>.
- [116] R. Zhou, T. Yu, X. Jiang, F. Chen, X. Zheng, Temperature-programmed reduction and temperature-programmed desorption studies of CuO/ZrO₂ catalysts, *Appl. Surf. Sci.* 148 (1999) 263–270, [https://doi.org/10.1016/S0169-4332\(98\)00369-9](https://doi.org/10.1016/S0169-4332(98)00369-9).
- [117] E. Lee, J. Lee, S. Hwang, D.H. Kim, Role of CeO_2 in promoting the spillover in CO oxidation reaction over platinum nanoparticle-supported CeO_2 catalyst, *J. Catal.* 417 (2023) 421–431, <https://doi.org/10.1016/j.jcat.2022.12.030>.
- [118] C. Ge, J. Sun, Q. Tong, W. Zou, L. Li, L. Dong, Synergistic effects of $\text{CeO}_2/\text{Cu}_2\text{O}$ on CO catalytic oxidation: Electronic interaction and oxygen defect, *J. Rare Earths* 40 (2022) 1211–1218, <https://doi.org/10.1016/j.jre.2021.08.014>.
- [119] Y. Zheng, K. Li, H. Wang, Y. Wang, D. Tian, Y. Wei, X. Zhu, C. Zeng, Y. Luo, Structure dependence and reaction mechanism of CO oxidation: A model study on macroporous CeO_2 and CeO_2 - ZrO_2 catalysts, *J. Catal.* 344 (2016) 365–377, <https://doi.org/10.1016/j.jcat.2016.10.008>.
- [120] G. Águila, F. Gracia, P. Araya, CuO and CeO_2 catalysts supported on Al_2O_3 , ZrO_2 , and SiO_2 in the oxidation of CO at low temperature, *Appl. Catal. A Gen.* 343 (2008) 16–24, <https://doi.org/10.1016/j.apcata.2008.03.015>.
- [121] J. Huang, S. Wang, Y. Zhao, X. Wang, S. Wang, S. Wu, S. Zhang, W. Huang, Synthesis and characterization of CuO/TiO₂ catalysts for low-temperature CO oxidation, *Catal. Commun.* 7 (2006) 1029–1034, <https://doi.org/10.1016/j.ccatcom.2006.05.001>.
- [122] Z.-Q. Zou, M. Meng, L.-H. Guo, Y.-Q. Zha, Synthesis and characterization of CuO/ $\text{Ce}_{1-x}\text{Ti}_x\text{O}_2$ catalysts used for low-temperature CO oxidation, *J. Hazard Mater.* 163 (2009) 835–842, <https://doi.org/10.1016/j.jhazmat.2008.07.035>.
- [123] T.-J. Huang, D.-H. Tsai, CO Oxidation Behavior of Copper and Copper Oxides, *Catal. Lett.* 87 (2003) 173–178, <https://doi.org/10.1023/A:1023495223738>.
- [124] I.V. Frishberg, Carbonyl Method of Metal Powder Production, in: *Handbook of Non-Ferrous Metal Powders*, Elsevier, 2009, pp. 154–162, <https://doi.org/10.1016/B978-1-85617-422-0.00007-0>.
- [125] K.H. Whitmire, Iron Compounds without Hydrocarbon Ligands, in: *Comprehensive Organometallic Chemistry II*, Elsevier, 1995, pp. 1–99, <https://doi.org/10.1016/B978-008046519-7.00056-3>.
- [126] J.A. Kerr, Bond Dissociation Energies by Kinetic Methods, *Chem. Rev.* 66 (1966) 465–500, <https://doi.org/10.1021/cr60243a001>.
- [127] S.W. Benson, III - Bond energies, *J. Chem. Educ.* 42 (1965) 502, <https://doi.org/10.1021/ed042p502>.
- [128] B. deB. Darwent, National Standard Reference Data Series, National Bureau of Standards, Washington, 1970.
- [129] T.L. Cottrell, *The Strengths of Chemical Bonds*, 2nd ed., Butterworth, London, 1958.
- [130] S.H. Oh, R.M. Sinkevitch, Carbon Monoxide Removal from Hydrogen-Rich Fuel Cell Feedstreams by Selective Catalytic Oxidation, *J. Catal.* 142 (1993) 254–262, <https://doi.org/10.1006/jcat.1993.1205>.
- [131] F. Zasada, J. Janas, W. Piskorz, M. Gorczyńska, Z. Sojka, Total oxidation of lean methane over cobalt spinel nanocubes controlled by the self-adjusted redox state of the catalyst: experimental and theoretical account for interplay between the langmuir–hinshelwood and mars–van krevelen mechanisms, *ACS Catal.* 7 (2017) 2853–2867, <https://doi.org/10.1021/acscatal.6b03139>.